ARTICLE

New modular organic platform for understanding the effect of structural changes on slow magnetic relaxation in mononuclear octahedral copper(II) complexes

Received 00th January 20xx,
Accepted 00th January 20xx

DOI: 10.1039/x0xx00000x

Dawid Marcinkowski[a#], Ariel Adamski[a#], Maciej Kubicki[a], Giuseppe Consiglio[b], Violetta Patroniak[a], Tomasz Ślusarski[a,c], Muhammed Açıkgöz[d], Daria Szeliga[e], Nahir Vadra[a,f], Mirosław Karbowiak[e], Ireneusz Stefaniuk[g], Czesław Rudowicz[a], Adam Gorczyński[a]* and Maria Korabik[e]*

Current advances in molecular magnetism are aimed at the construction of molecular nanomagnets and spin qubits for their utilization as high-density data storage materials and quantum computers. Mononuclear coordination compounds with low spin values of S=½ are excellent candidates for this endeavour, but their construction via rational design is limited. This particularly applies to the single copper(II) spin center, having been only recently demonstrated to exhibit slow relaxation of magnetisation in the appropriate octahedral environment. We have thus prepared a novel, modular organic scaffold that would allow one to gain general insight into how purposeful structural differences affect the slow magnetic relaxation in monometallic, transition metal complexes. As a proof-of-principle, we demonstrate how one can construct two, structurally very similar complexes with isolated Cu(II) ions in an octahedral ligand environment, the magnetic properties of which differ significantly. The differences in structural symmetry effects and in magnetic relaxation are corroborated with a series of experimental and theoretical techniques, showing how symmetry distortions affect the relaxation behaviour in these isolated Cu(II) systems. Our highly modular organic platform can be efficiently utilized for the construction of various transition-metal ion systems in the future, effectively providing a model system for investigation of magnetic relaxation via targeted structural distortions.

1. Introduction

Molecular nanomagnets (MNMs) are the focus of scientists due to possibility of use in a variety of applications[1-4], including molecular spintronics[1, 5, 6], high-density information storage[7-9] , quantum information processing or sensing.[10-16] These systems display magnetic hysteresis below their blocking temperature (T_B) and are magnetically bi-stable, exhibiting an energy barrier to spin reversal (U_{eff})[17-22], ultimately manifested by macroscopic quantum tunneling and slow relaxation of magnetization. Among the many types of MNMs three major groups of coordination compounds based on transition ions play central role. They encompass: the single-molecule magnets (SMMs) and single-chain magnets (SCMs), which belong to specific class of exchange coupled systems as well as the single-ion magnets (SIMs), which are mononuclear complexes.[3, 19, 22-27] The first example of a SMM was a $[Mn_{12}O_{12}(OAc)_{16}(H_2O)_4]\cdot 2MeCO_2H\cdot 4H_2O$ cluster synthesized by Lis[28] and magnetically characterized after 11 years by R. Sessoli, D. Gatteschi et al., which exhibits U_{eff} = 60 K and T_B=3K.[29] That discovery was the birth of SMMs chemistry and the beginning of the search for a holy grail of molecular magnetism, which is a SMM system with a T_B above room temperature. The interests towards this field focused principally on high nuclearity *d*-block[30] and then *f*-block[31, 32] systems with large spin ground states, nevertheless in recent years, research concentrates on single-ion systems of the *f*-[33-36] and *d*- block[37, 38] elements. Challenges that have emerged in the field SMMs were to understand and control the magnetic anisotropy, leading to higher values of both U_{eff} and T_B. Nowadays, the highest T_B has been reported by Guo et al.[39], where dysprosium compound displays magnetic hysteresis at temperatures reaching 80 K. That discovery theoreticaly overcomes an essential barrier toward the development of

[a] Faculty of Chemistry, Adam Mickiewicz University, Uniwersytetu Poznańskiego 8, 61-614 Poznań
[b] Dipartimento di Scienze Chimiche, Università di Catania, I-95125 Catania, Italy
[c] Institute of Spintronics and Quantum Information, Faculty of Physics, Adam Mickiewicz University, Uniwersytetu Poznańskiego 2, 61-614 Poznań, Poland
[d] Department of Science, The State University of New York (SUNY) Maritime College, New York 10465, USA
[e] Faculty of Chemistry, University of Wrocław, F. Joliot-Curie 14, 50-383 Wrocław, Poland
[f] Universidad de Buenos Aires, Facultad de Ciencias Exactas y Naturales, Departamento de Química Inorgánica, Analítica y Química Física and CONICET–Universidad de Buenos Aires, Instituto de Química Física de los Materiales, Medio Ambiente y Energía (INQUIMAE), Buenos Aires C1428EGA, Argentina
[g] College of Natural Sciences, University of Rzeszow, Rejtana 16a, 35-310 Rzeszow, Poland
#Ariel Adamski and Dawid Marcinkowski contributed equally. Electronic Supplementary Information (ESI) available: experimental synthetic details, part of magnetic, spectroscopic and theoretical details. See DOI: 10.1039/x0xx00000x

Please do not adjust margins

molecular magnetic devices that function at liquid nitrogen temperatures. Unfortunately, subsequent studies with various Dy(III) congeners of this family[40-42] show that U_{eff} and T_b are not simply correlated with the Dy-X distance and X-Dy-X angle axiality (where X – donor atom(s)) and that particular attention should be also devoted to magnetization relaxation mechanisms.[4, 43-49]

Although the first *d*-block SIM was presented by Koga and co-workers[50] in 2003, real interest in the subject of SIMs began after the publication of work by Long and co-workers[51], who described nonheme trigonal pyramidal Fe(II) system exhibiting slow magnetic relaxation. Thereafter there has been an increasing number of first-row *d*-block SIM systems reported in the literature, with Co(II)[52-56] and Fe(I/II/III)[57-60] based systems having dominated the field of 3*d* molecular magnets.[61] But other low-spin d^n systems were also studied with notable input given towards understanding how to construct magnetically relevant systems based on monometallic coordination compounds. Whittlesey and co-workers[62] demonstrated the use of bulky *N*-heterocyclic carbene ligands to synthesize a two-coordinate d^9 Ni(I) complex to display SIM behavior. Other d^9 Ni(I) systems were proposed by Lin et al.[63], where the influence of distortions on magnetic properties were shown. At the same time Titiš and co-workers[64] reported the first example of a mononuclear d^8 hexacoordinate Ni(II) complex [Ni(pydc)(pydm)] (pydc = pyridine-2,6-dicarboxylate, pydm = 2,6-bis(hydroxymethyl) pyridine), demonstrating that low coordination number geometries are not a prerequisite for SIM behavior. Bhowmick et al.[65] reported first example of SIM behavior in d^7 Ni(III; S = ½) complexes. Cui[66] introduced a new approach, where slow magnetic relaxation originates from the low spin state of d^7 Co(II; S = ½) ions. For this systems, Chen[67] reported, that the spin–orbit coupling plays a crucial role in stabilizing an anisotropic ground doublet, resulting in the SIM behavior. Furthermore d^3 Fe(V; S = ½)[68] and Mn(IV; S = ½)[69] complexes were shown, in which Jahn-Teller (J-T) distortion lowers the molecular symmetry, but does not completely quench spin – orbit coupling.[70] Different example associated with J-T distortion, but not with the same total spin is Mn(III) complex, where photoexcitation can strongly influence its symmetry, which is responsible for magnetic properties.[71] Above examples show that the symmetry distortions are crucial to affect the magnetic properties.

It was noted that for such systems to exhibit qubit behavior and/or SIM characteristics, the following is preferred: (i) square planar coordination geometry; (ii) coordinating atoms devoid of nuclear spin; (iii) rigidification of the molecular architecture; (iv) minimization of the protons influence above a certain radius from the metal (the concept of spin diffusion barrier.[14, 72-74] Although significant information can be extracted from the studies on the related S=½ V(IV) complexes[73, 75-81], examples of compounds with experimentally determined field-induced slow magnetic relaxation with single d^9 Cu(II, S = ½) ion are very scarce[82-85] and their origin is not fully understood.[23, 24] Notably, examples of d^9 Cu(II) systems proposed to act as potential spin qubits were phthalocyanines[86, 87], porphyrines[72, 88-90] and

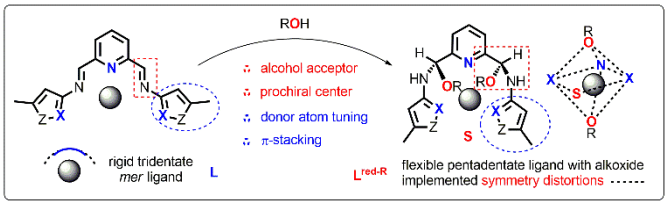

Scheme 1. Schematic representation of the rationale behind the modular organic platform designed and implemented in the present studies for monometallic magneto-structural correlations.

oxygen (acetylacetonates) or sulphur (dithiocatecholates) ligating species.[91-93] Recent record value of 1.4 ms coherence time was demonstrated by Dai et al.[91] for a $(PPh_4)_2[Cu(mnt)_2]$ (where mnt^{2-} is maleonitriledithiolate), after dilution in isostructural diamagnetic Ni(II) matrix and utilization of dynamic decoupling technique. Nonetheless, more studies on Cu(II)-based systems are needed to gain deeper understanding of magneto-structural correlations that determine observation of these phenomena as well as the underlying relaxation mechanisms.

Modular organic platforms that can be utilized for determination of magneto-structural correlations are difficult to construct, nonetheless they would be ideal for prediction of magnetic parameters based on the structural parameters alone.[23] We therefore present unique example of such system, which is suitable for construction of monometallic transition metal complexes, the structure of which can be carefully altered within the ascertained symmetry regime. (Scheme 1)

Herein, the synthesis, structural and magnetic characterization as well as optical and EMR/EPR spectroscopy measurements of two structurally similar complexes is presented, which are formed in reaction of the pyridine/isoxazoline ligand **L** with $Cu(ClO_4)_2{\cdot}6H_2O$ **1** and $Cu(OTf)_2$ **2** salts. Unexpectedly, *in-situ* reduction of the imine ligand **L** occurs, effectively providing two monometallic copper(II) complexes with the pentadentate $\mathbf{L^{red\text{-}R}}$ ligand with the chiral *N*,*O*-aminal motif. The final structures and the resulting symmetry can be fine-tuned by the synthetic conditions, principally via the choice of the alcohol in the reaction medium. The influence of the ligand surrounding on the static and dynamic magnetic properties of Cu(II) ions in these complexes was discussed and compared with the previously studied monometallic copper(II) systems that exhibit slow magnetic relaxation. To explain and corroborate the values of the quantities measured experimentally we have set out for extensive computational studies utilizing density functional theory (DFT)/*ab initio* and semiempirical approaches. As a case study for these computations, the experimental data reported herein are utilized.

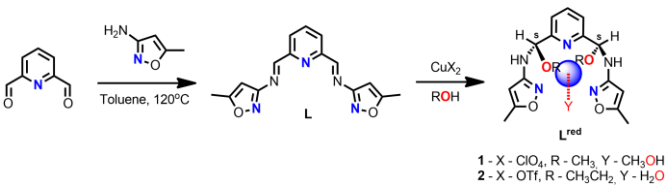

Scheme 2. Synthetic pathway leading to Schiff base ligand **L** and its copper(II) complexes; blue sphere represents Cu(II) ion.

2. Results and discussion

2.1 Synthesis

The ligand **L** was synthesized via condensation of 2,6-pyridinedicarboxaldehyde with 3-amino-5-methylisoxazole as presented in Scheme 2. Although **L** was isolated and characterized (see Section II in SI), its complexation with CuX_2 salts in the presence of alcohols leads to unexpected structural transformations. Reactions of $Cu(ClO_4)_2{\cdot}6H_2O$ **1** and $Cu(OTf)_2$ **2** salts with isolated Schiff base ligand **L** lead to the asymmetric addition of MeOH **1** or EtOH **2** to the imine bond, resulting in the formation of chiral *N,O*-aminal $\mathbf{L^{red\text{-}R}}$, which is unambiguously established via X-ray crystallography of isolated coordination compounds **1** and **2** (Table S1; Section 2.2). Whereas reduction of the parent ligand **L** is most plausibly facilitated by the template effect of Cu(II) ions, it is yet to be determined if such reaction is diastereospecific or one of the chiral isomers (here *S,S*) crystallized in the preferential manner. The solvent as well as the counter ions OTf^- and ClO_4^- does not seem to affect the type of isomer obtained in both structures. Such chiral *N,O*-aminal motif is found in a number of natural, pharmaceutical products and valuable synthetic precursors[94-96], therefore, the development of effective and effortless methods for their synthesis has attracted considerable research effort.[97, 98] This report is the first on the formation of aldimine-derived *N,O*-aminals, without the need of applying the external chiral catalyst. Interestingly, only three studies[97, 99, 100] on the use of metallic catalysts in the formation of *N,O*-aminals from related ketimines were reported. Altogether, our approach can be used to form chiral molecules with the N,O-aminals, strategically placed at the 2,6-positions of pyridine, of potential use in construction of more complex systems, particularly of biological or magnetic relevance.

2.2 Structural characterization of Cu(II) complexes

Figure 1a,b shows the perspective views of molecules **1** (a) and **2** (b) together with the numbering schemes. Table S2 lists the relevant geometrical parameters. Pentadentate ligands $\mathbf{L_{red}^1}$ (ClO_4^-; MeOH)and $\mathbf{L_{red}^2}$ (OTf^-, EtOH) wrap around copper(II) ions and differ by either methoxy (**1**) or ethoxy (**2**) groups attached to the stereogenic center, as a result of the unexpected addition of alcohol to the imine bond (Scheme 2). In both crystal structures complexes exist as dications, with two perchlorate (**1**) or triflate (**2**) anions balancing the charge. Cu(II) centers are six-coordinated in distorted octahedral fashion (Figure 1c). Due to the structure of the ligand the octahedra are elongated along one direction (O7···O14), and this elongation is as large as 25% in **1** and slightly smaller in **2** (Figure 1c,d). Such an elongation may be in part responsible for specific anisotropy of magnetic properties. Such a geometry is related to the conformation of ligand molecules, in which the ring planes are almost perpendicular one to another (Table S2). This also results in an almost square planar character of the tetradentate plane from three nitrogen atoms of the $\mathbf{L^{red\text{-}R}}$ ligand and the oxygen atom from the solvent molecule (see SHAPE analysis in Section 2.3). In the crystal structure of **1** there are infinite chains of alternate cations and anions connected by the hydrogen bonds, with the second anion threaded to this chain (Figure S1 (left), (Table S3). In **2**, the main structural motif is a cluster of hydrogen bonded structural fragments: two cations, four triflate anions, and two solvent-ethanol molecules (Figure S1 (right)). These principal motifs are connected to form the three-dimensional crystal structure by means of electrostatic interactions and weak intermolecular van der Waals forces. Different H-bonding patterns are also responsible for changes in the electronic dipole character of the coordinated solvent molecule (MeOH in **1** and H_2O in **2**) which can theoreticaly affect the magnetic properties as well.

2.3 SHAPE analysis

To gain more insight into the local site-symmetry in **1** and **2**, calculations using SHAPE software[101, 102] were performed, which utilize the continuous shape measurements (CShM)[103] method. S parameter is therefore introduced, which corresponds to the degree of deviations from the perfect polyhedron with $S = 0$ corresponding to ideal geometry. Results shown in Table S4 clearly indicate that **1** and **2**, as well as magnetically relevant Cu(II) system studied by Boca[82] show significant deviations from the octahedral geometry, classified as structurally severe distortions ($S > 3$).[101] Considering that observation of slow magnetic relaxation in Cu(II; $S = ½$) systems should be related to the deviations from idealized symmetry, one can relate the differences in S-value to slower (**1**) or faster (**2**) relaxation of magnetization (see *AC* studies in Section 2.5). Although it is not very high (ca. 0.2), the chemically significant differences were classified to be visible from 0.1 value changes.[101] Though more examples of octahedral Cu(II) ions that exhibit slow relaxation of magnetization would have to be studied beforehand, we hypothesize that based on Table S4, octahedral distortions characterized by S-value = ca. 3.7 value might be the limiting factor when the onset of the magnetic relaxation is observed. This would mean that for isolated Cu(II) ions in an octahedral

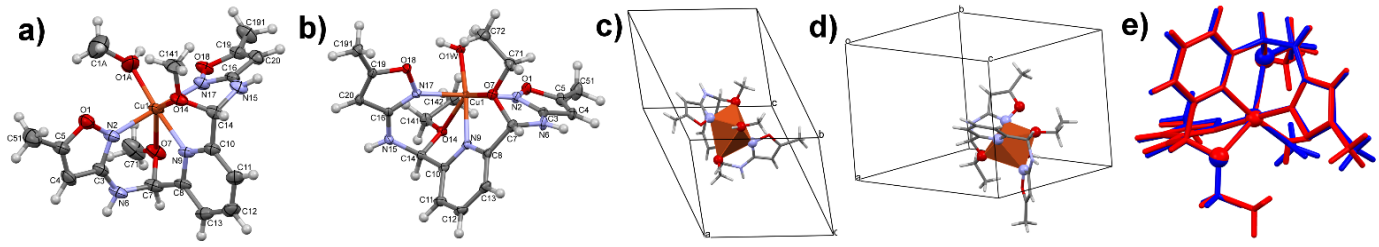

Figure 1. Perspective views of dicationic complexes **1** (a) and **2** (b). Ellipsoids are drawn at the 50% probability level, hydrogen atoms are shown as spheres of arbitrary units; The orientations of long axis of the coordination octahedron in **1** (c) and **2** (d); (e) Superimposed structures of dicationic complexes **1** (blue) and **2** (red).

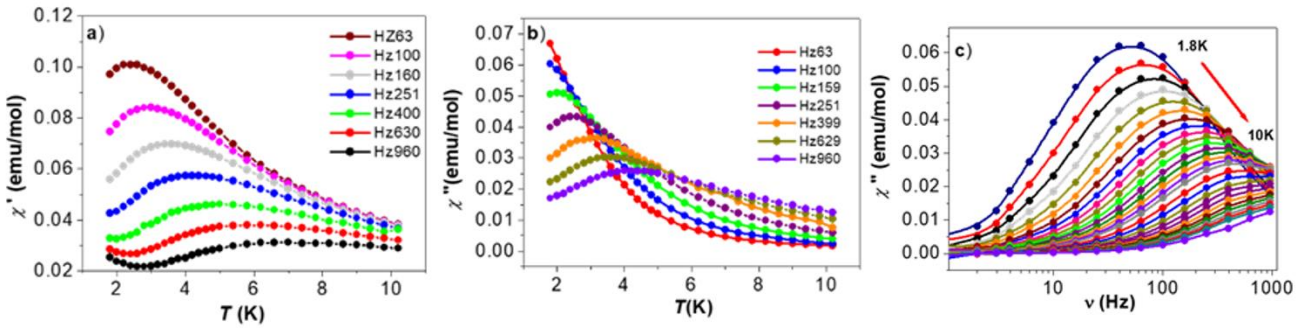

Figure 2. Temperature dependence of: a) the in-phase χ', b) the out-of-phase χ'' susceptibility and c) χ'' vs frequency for compound **1**.

m environment, any distortions smaller than that would result in lack of this magnetic phenomenon.

Given that investigated systems are heterotopic in terms of ligands nature (N and O donor atoms), we performed additional analysis regarding square planar planes present in the studied octahedra. The aim was to understand: (i) which part of the ligands architecture is responsible for structural anisotropy of relevance to magnetic properties and (ii) why do the observed magnetic properties differ in **1** and **2**. Results are gathered in Table S5. One can discriminate three planes: (A) (N2-N9-N17-MeOH/H_2O) which is dependent on the monodentate MeOH (**1**) or H_2O (**2**) solvent molecules; (B) (MeOH/H_2O-N9-O7-O14) and (C) (N2-N17-O7-O14) which are mostly influenced by the O7-O14, distortions. Unexpectedly, it appears that plane (A) alone would favor a significantly higher distortion degree in compound **2** (S-value **2** = 0.308 vs S-value **1** = 0.077). This should also dependent on the H-bonding pattern with the perchlorate (**1**) or triflate (**2**) counterions. S-values in planes (B) and (C) favour stronger distortions in **1** than in **2**, ascribed to the plane formed by isoxazole/alkoxide moieties.

From the structural point of view, we hypothesize that the difference in the magnetic properties of **1** and **2** are related to: (i) the reduced octahedral distortions in **2** when compared to **1** as well as (ii) higher deviation from the square planar character within the N3O plane for **2** than in **1**. Interestingly, although the monodentate coordination of H_2O results in higher deviation from the NNN-OH_2 plane in **2** than chemically equivalent NNN-(OH)Me in **1**, this effect seems to be more profound than distortions in the planes (B) and (C) associated with coordinating methoxy/ethoxy moieties of the reduced ligand. This can be understood when considering that the spin-active nitrogen atoms have the negative effect on the SIM/qubit behaviour[72, 73], which is however minimized within the square planar coordination environment.

2.4 DC magnetic properties

The magnetic properties of powdered microcrystalline samples **1** and **2** were studied by measuring the thermal dependence of the magnetic susceptibility in the temperature range of 1.8 – 300 K and magnetic field of 0.5 T. The field dependences of the magnetization from 0 to 5 T for **1** and **2** were measured at 2 K.

In DC magnetic field both compounds show similar properties, typical for non-interacting S = ½ spin system (Figure S2). The $\chi_m T$ product values (0.373±0.005 cm^3Kmol^{-1}, μ_{eff} = 1.73±0.01 B.M.) are practically constant in the whole measured temperature range 1.8 - 300 K. The $1/\chi_m$ versus T plots obeys the Curie-Weiss law with Curie constant C = 0.384 and 0.393 cm^3Kmol^{-1} and Weiss constant θ = -0.1 and -0.3 K for **1** and **2**, respectively. Simulation of magnetic susceptibility curves using molecular field correction:[104, 105]

$\chi_m = \frac{\chi}{\left(\frac{2zJ'}{Ng^2\beta^2}\right)\chi}$ incorporated in the PHI program[106] yields very low parameters: zJ' = -0.05 and -0.10 cm^{-1} for **1** and **2**, respectively. This finding confirms that Cu(II) centers are practically magnetically isolated in both compounds, in accordance with determined X-ray structures (see Section 2.2). Hence the effect of exchange coupling between Cu(II) ions may be excluded. Magnetically isolated Cu(II) ions in the crystal structure of **1** and **2** are also confirmed by magnetization versus field measurements measured at 2 K (Figure S3). Experimental points agree with the Brillouin function for S = ½ and g = 2. The goodness of agreement factor R, defined as:

$$R = \sum_{i=1}^{n} \frac{(\chi_i^{exp}T - \chi_i^{calc}T)^2}{(\chi_i^{exp}T)^2}$$

was obtained as: R = $4.43 \cdot 10^{-6}$ and $2.02 \cdot 10^{-6}$ for **1** and **2**, respectively.

2.5 AC magnetic properties

Measurements were made at $3 \cdot 10^{-4}$ T oscillating field for 16 frequencies, in the temperature range 1.8 – 10 K. An external magnetic DC field of 0.1 T was chosen from the maximum of out of phase susceptibility χ'' versus magnetic field relation (Figures S4 and S5). Please notice that much stronger field must be applied for compound **2** than for **1**, which also correlates with more pronounced character of slow magnetic relaxation in AC field for the latter one (*vide infra*). The AC susceptibility measurements reveal surprising finding. The out of phase component χ'' of **1** and **2** is silent at zero DC field, which indicates that the magnetization relaxation time (τ) is much shorter than ½πν of the AC field. Measurements done under 0.1 T Dc field reveal differences in properties of compounds **1** and

2. The in-phase χ' (Figure 2a) and out-of-phase χ'' (Figures 2b,c) susceptibilities show temperature and frequency dependence with characteristic maxima in **1**, indicating the slow magnetic relaxation phenomenon. Different types of relaxation mechanisms can be potentially involved in molecular system: Orbach, direct, Raman, and quantum tunneling (QTM) components, respectively).[82, 83]

$$\tau^{-1} = \tau_0^{-1} \exp\left(-\frac{U}{k_B T}\right) + aT + bT^n + \tau_{QTM}^{-1}$$

In the literature, one can find different approaches to the Arrhenius equation:

$$\tau^{-1} = \tau_0^{-1} \exp\left(-\frac{U}{k_B T}\right)$$

performed in AC magnetic field studies for the relaxation processes observed for coordination compounds with spin S = ½. Some authors suggest that τ does not follow the Arrhenius behavior, because of lack of magnetic states besides m_S=±½ doublet that can be thermally populated providing a path for the multiphonon Orbach mechanism of relaxation. Consequently, they propose to use Raman and direct mechanisms, which dominate at high and low temperature respectively.[75-77] Other authors, such as Boca et al [54], use Arrhenius-like plot to determine activation energy of the relaxation process U/k_B and τ_0, admitting that effective energy barrier from zero-field splitting of the ground term does not exist in the Cu(II) system. It results in elimination of the Orbach mechanism in relaxation process in S = ½ compounds. The analysis of the relaxation process of **1** was carried out using:

Table 1 Fitting of different relaxation parameters of compound **1** determined from AC studies based on Figure 3a.

Relaxation mechanism	b (s^{-1} K^{-n})	n	a (s^{-1} K^{-1})	τ_{QTM} (s^{-1})	Discrepancy factor R
Raman+direct+QTM	18.59(2)	1.32(1)	1.06(2)	0.46(2)	$4.05 \cdot 10^{-5}$
Raman+direct	18.78(1)	1.33(2)	3.66(2)		$4.05 \cdot 10^{-5}$
Raman	68.76(1)	2.32			

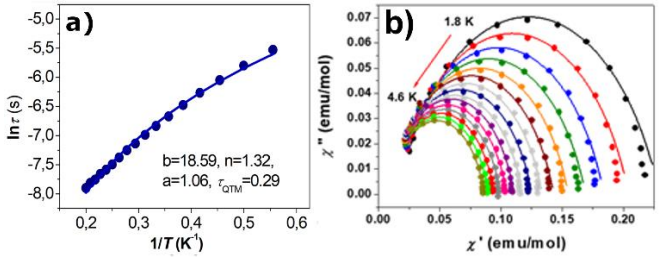

Figure 3. (a) Magnetization relaxation time ln(τ) in a function of reciprocal temperature T^{-1} of **1**. The effect of using Raman + direct + QTM in fitting procedure is presented in the form of a continuous line; (b) Cole–Cole plots for **1** under 0.15 T dc field. The solid lines are the best fits to the experiments with the generalized Debye model.[64]

a) the Raman mechanism itself; b) Raman and direct processes; c) Raman, direct and QTM relaxation modes, knowing that Raman mechanism plays a dominant role in S=½ system.[76] The τ^{-1} vs T dependence is almost linear, what suggests that direct relaxation mechanism cannot be ignored.[76] The matching results of fitting are shown in the Table 1 and in Figure 3a. Accounting only the Raman mechanism gives a good fit but too high a value of b=68.76. Calculation with Raman and direct mechanisms as well as Raman, direct and QTM gave parameters b=18.59 s^{-1} $K^{-1.32}$, n=1.32, a=1.06 and QTM equal 0.46, similar to those found for S = ½ spins in Cu(II) complexes. [83] Authors of [83] finally proposed Raman-like process is operative in spin-lattice relaxation in analyzed five coordinated Cu(II) complex. In the Raman process, relaxation follows through a virtual state. The direct process describes relaxation from −½ to +½ states with emission of a single lattice phonon. Relaxation through QTM is facilitated by the anisotropy of the system.[54]

The Cole–Cole plots from the *AC* magnetic susceptibility data of **1** (Figure 3b) were fitted by the generalized Debye model (Table S6).[107, 108] The α parameters describing the distribution of the relaxation times in a magnetic system were extracted. The limiting value of α = 0 describes a single relaxation process, whereas α = 1 corresponds to an infinitely wide distribution of the relaxation times. The wider the distribution of the relaxation times, the larger the value of α.[107,87] A small value of the distribution coefficient α (0.16 at 4.4 K to 0.25 at 1.8 K) for complex **1** indicates that the relaxation process has a narrow distribution of relaxation time. The τ parameters were extracted from the Debay model (Figure S6), with τ = 3.97 ms at 1.8.K. Similar temperature relations and values were presented for vanadium(IV)-based compounds, with S=½.[109]

AC susceptibility measurements of compound **2** differ from **1**, with no phase shift maxima present in the in-phase χ' vs T dependencies (Figure 4a) and only the slight onset of the out-of-phase signals χ'' vs T (Figures 5b and c) under high external magnetic field frequencies. Despite high structural resemblance of the Cu(II) coordination environment, the properties of **1** and **2** differ significantly and this precluded us from determination of the relaxation parameters for compound the latter one. Only two examples of field induced Cu(II) SIM behavior have been reported so far.[82, 83] Boča et al.[82] showed that octahedral [Cu(pydca)(dmpy)]·0.5H_2O (where pydca - pyridine-2,6-dicarboxylate, dmpy - 2,6- dimethanolpyridine) exhibits two relaxation processes with energy barriers estimated as U_{eff}/k_B = 58.6 and 62.7 K (possibly as a result of two distinct, symmetry differentiated Cu(II) in the crystal lattice). Cui et al.[83] showed that five-coordinate [Cu(12-TMC)Cl][$B(C_6H_5)_4$] (12-TMC = 1,4,7,10-tetramethyl-1,4,7,10-tetraazacyclododecane) exhibits only one relaxation process in a distorted square pyramidal geometry of copper(II) ion.

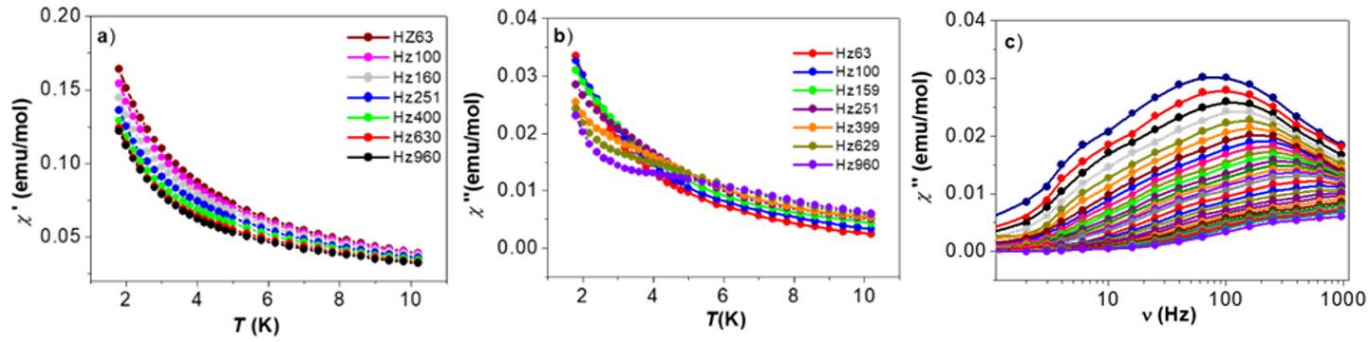

Figure 4. Temperature dependence of: a) the in-phase χ', b) the out-of-phase χ'' susceptibility and χ'' vs frequency dependence of the compound **2**.

Authors also show[83] that the anisotropy of spectroscopic splitting factors g_i had decisive influence on magnetic relaxation, which correlates with our studies (see Section 2.6).

2.6 CW-EPR and pulsed EPR studies

Continuous wave electron paramagnetic resonance (CW-EPR) spectra were recorded in X and Q band frequencies to corroborate magnetic phenomena (Sections 2.4 and 2.5) with structural studies (Sections 2.2 and 2.3), whereas the pulsed variant of the method allowed to better understand the spin-lattice magnetic relaxation processes. For experimental details see EPR Section III in the SI. CW-EPR spectra of compounds **1** and **2** down to liquid nitrogen (X-band) and helium (Q-band) temperatures with fitting protocols are presented in the SI (Figures S7-S16), while representative ones are in Figure 5. The spectroscopic splitting factors $g_\perp$ and $g_\parallel$ for all spectra are presented in Table 2 and prove their axial character type ($g_\parallel > g_\perp$). Transition energy levels at the resonance field B_{res} are presented in Tables S7 and S8 and their graphical representation in Figures S17 and S18.

Room temperature X-band EPR spectra of **1** and **2** (Figure 5 top) are temperature-independent down to 77K. For **1** the axial type spectrum spectrum is partially, but clearly resolved with spectroscopic splitting factors $g_\perp$ = 2.06, $g_\parallel$ = 2.28 and parallel hyperfine splitting parameter $A_\parallel$ = 175 G, resulting from the interaction of the unpaired electron of Cu(II) with the spin of copper nucleus $I = 3/2$. It is identical for both natural isotopes of ^{63}Cu and ^{65}Cu, so eight hyperfine levels can be expected with four allowed transitions: $\Delta M_S = \pm 1$ and $\Delta M_I = 0$ (Figure S19).[110] The axial EPR spectrum of compound **2** exhibits similar values of spectroscopic splitting parameters $g_\perp$ = 2.06 and $g_\parallel$ = 2.25 but with no hyperfine structure. From spectra in Q-band valuable information can be obtained, because the hyperfine structures are more pronounced for both compounds and it can be also observed for compound **2**, which was not the case for X-band frequencies. Down in helium temperatures, formation of a bimodal peak is observed for compound **1** in the range of 1200—1300 mT magnetic field. The second line is and image of

Table 2. The fitted SH parameters: Zeeman factors (g_i; dimensionless), hyperfine interaction (A_i; in 10^{-4} cm^{-1}) and spectral parameters for compounds **1** and **2**.

Cmpd	1				2			
EPR band	X	Q	X	Q	X	Q	X	Q
T[K]	300	180	90	10.5	300	300	91	11
g_1	2.029	2.048	2.035	1.950	2.059	2.053	2.060	2.012
g_2	2.071	2.040	2.063	2.029	2.059	2.053	2.062	2.067
g_3	2.259	2.258	2.258	2.289	2.32	2.307	2.185	2.349
$[g_3-g_1]$	0.230	0.210	0.223	0.339	0.261	0.254	0.125	0.337
A_1	-4.79	2.739	-3.33	23.34	-1.756	-0.0002	-0.0002	36.69
A_2	-0.37	-25.47	3.2E-05	-0.116	-0.232	0.0034	0.0002	-60.04
A_3	179.73	184.5	187.52	206.8	128.7	141.7	102.80	240.2
Lwpp [mT]	10.022	12.21	10.98	15.98	6.35	8.95	6.39	18
RMSD*	0.005	0.011	0.010	0.056	0.031	0.032	0.028	0.11

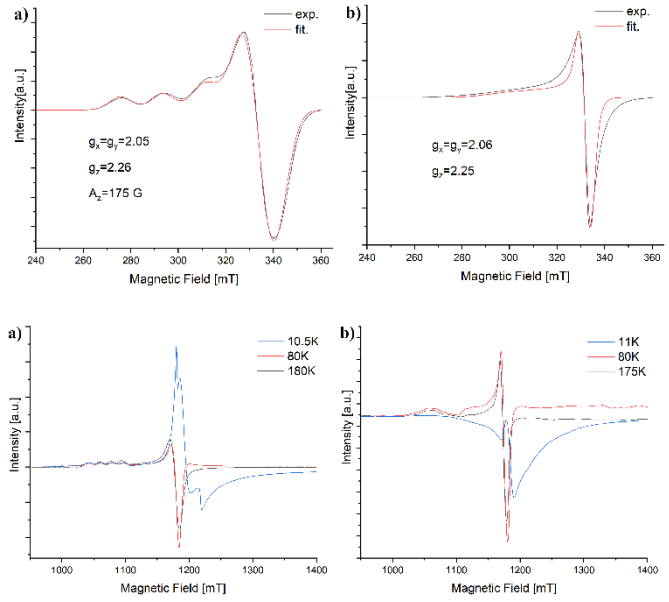

Figure 5. Top: X-band EPR spectra of **1** (a) and **2** (b) at RT; solid red line shows temperature independent simulated spectrum with parameters presented. The same type of spectrum with the same parameters were observed at 77K; bottom: superposition of Q-band spectra of **1** (a) and **2** (b) at chosen temperature intervals: representative simulated spectra are shown in the SI.

transitions in the perpendicular direction (i.e. xy‖B), this effect is clearly observed for sample **1**, while for sample **2** it is less apparent due to larger line widths. The phenomenon is even more visible in temperature-dependent EPR spectra (Figures S7 and S8) which can be attributed to different orientations of molecules in crystal lattice relative to the magnetic field but would also depend on the structure of individual compounds. In addition, the LFMA (Low Field Microwave Absorption) line, which is an indicator of ferromagnetic interactions, does not occur even up to helium temperatures for both tested samples. This means ferromagnetic interactions are not present in **1** and **2**, which is consistent with the DC susceptibility studies (see Section 2.4).

In the systems where the D parameter cannot be assigned (S = ½) it is possible to predict the presence of magnetic anisotropy based on the [$g_z - g_x$] difference.[82] The values (Table 2) for **1** and **2** are three times higher than for the related system presented in the literature, which indicates that it can be exploited in quantifying the magnetic anisotropy. Nevertheless, since at liquid helium temperatures [$g_z - g_x$] values are similar for **1** and **2**, it is not the only parameter that should be considered to explain the magnetic behavior (with magnetic relaxation being much longer for **1** than in **2**). One can also observe that temperature significantly influences the g_{eff} factor (Figure S20) and the EPR line width B_{pp} (Figure S21) for both compounds down to the liquid helium temperatures.

The in-depth structural analysis for both compounds shows that although they are sufficiently separated to exclude coupling for **1** there are two opposite centers exactly inverted and the pairs are perfectly parallel. For **2** they are also inverted, but the pairs are not parallel (Figure S22). Additionally, position of pyridine rings in **1** is very similar to those presented in the publication[64], while for **2** their somewhat equivalent role is taken by the five-membered oxazole rings. These structural differences can also contribute to the differences in the observed EPR spectra between **1** and **2**. SHAPE analysis (see Section 2.3) also shows that for **1** the deviations for the plane N2-N9-N17-MeOH from the perfectly square planar disposition are significantly smaller than in compound **2**, which is most preferred for QIP systems.[72, 73]

To gain insight into relaxation processes of the compounds, we performed the pulsed EPR spectra in Q-band down to liquid helium temperatures. The relaxation time T_1 determined for both compounds are presented in Figures S23 and S24. For compound **1**, the T_1 increase very fast in range of 28-34K, but similar behavior is observed in different S=½ systems.[92, 111] For **2** the behavior is different and we observe a shortening of T_1 with increasing temperature. The inverse spin-lattice relaxation ($1/T_1$) model (Figure S25 and EPR Section III in SI) allowed us to assign two processes (Raman and direct) having the greatest impact on relaxation, what correlates well with the AC magnetic susceptibility studies (Section 2.5).

2.7 Theoretical calculations of spin Hamiltonian parameters

Using PHI program[106] we simulated EPR spectra and variation of electronic levels with external magnetic field for compound **1**.

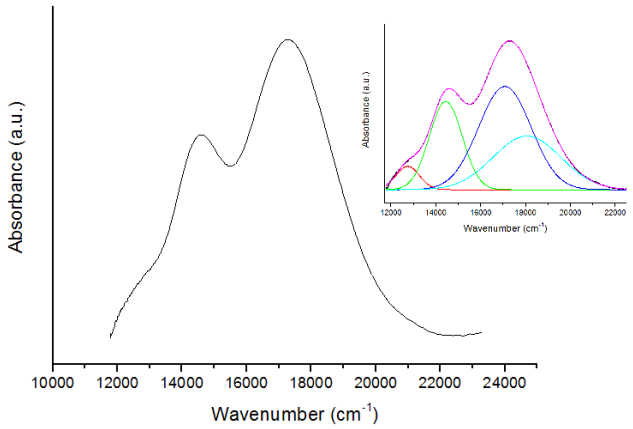

Figure 6. Absorption spectrum of **1** in the range of Cu(II) electronic transitions at 4.2 K.

To simulate Cu(II) ion we set spin S as ½ and orbital quantum number L as 2. Spin Hamiltonians (SH) parameters (Section 2.9) were calculated using MOLCAS[112] and we take g_x = 2.0660, g_y = 2.0920, g_z = 2.3810 from NEVPT2 calculations (Section 2.9). Temperature was set at 300 K, field frequency at 10 GHz (X-band), field was swept from 0.25 to 0.4 Tesla and was directed along the x-, y-, and z-axis of g-tensor as well as powder integration was used. We used anisotropic spectra line widths to get better resemblance to experimental fits. Observed anisotropic broadening (Figures S26, S27) might correspond to unresolved spectral features such as hyperfine coupling[113, 114] and correlates with the experimentally observed structure.

2.8 Optical spectroscopy

To gain more insight into the electronic levels of **1** and therefore the nature of observed slow magnetic relaxation, optical spectroscopy and superposition model (SPM) calculations were performed. Figure S28 shows the absorption spectrum measured at RT for complex **1**. The intense bands observed in the range of 22,000 - 50,000 cm^{-1} are associated with ligand-centered transitions. Electronic transitions of Cu(II) ions are much less intense than those associated with ligand absorption. They appear clearly for a more concentrated sample (blue line) and are observed in the range of 12,000 – 21,000 cm^{-1}. Figure 6 shows the absorption spectrum recorded in the range of Cu(II) electronic transitions at 4.2 K. Two bands at approximately 14,600 and 17,300 cm^{-1} and a shoulder at approximately 12,600 cm^{-1} are clearly visible.

The nearest surrounding of Cu(II) ion in **1** is formed by 3 N atoms and 3 O atoms and the actual site symmetry of Cu(II) center is C_1. The Figure S29 shows, that appropriate selection of (x, y, z) axis system (see Section IV and Table S9) allows to approximate the actual symmetry with C_2 symmetry. The axis system (x, y, z) was selected with the origin (0, 0, 0) on the Cu atom, the oxygen atom O1A on the z axis, the N2 and N17 atoms almost exactly on the x axis (angle θ = 90.60°). The coordination polyhedron of Cu(II) ion can be also considered as a distorted octahedron (Sections 2.2 and 2.3). The major deviation from the ideal octahedron results from position of O7 and O14 atoms. The angles O7-Cu-O1A and O14-Cu-O1A are 111.13° and 104.56°,

respectively, and the angles O14-Cu-N2 and O7-Cu-N17 are 99.92° and 97.12°, respectively, whereas for perfect octahedron all angles should be equal to 90°. Moreover, the Cu-O14 and Cu-O7 distances (238.8 and 248.9 ppm) are larger than distances between Cu and other atoms, which are very similar and confined within 195.6 pm (Cu-O1a) - 199.6 pm (Cu-N9) range. This is also corroborated by the SHAPE calculations from the analysis of the deviations from the square planar planes. From the three planes that can be constructed from the octahedral geometry by elimination of axial ligands, the highest S value corresponds to the N2-N17-O7-O14 planes, both for compound **1** and **2** (Tables S4 and S5). Comparison of deviation between **1** and **2** in this plane is higher for **1** (4.669 vs 4.172) and this falls in line with the results of magnetic studies *i.e.* that slow magnetic relaxation for the triflate analogue **2** is much faster than in the case of **1**. In addition, the deviation of the N2-N9-N17-MeOH/H_2O planes is also higher and should contribute to the observed magnetic phenomena. Nevertheless, in spite of this deviation the use of the symmetry descent scheme O_h -> D_{4h} -> C_2 for rationalization of absorption spectrum of **1** is fully justified. In the hole formalism the degenerate 5*d* levels of $3d^9$ configuration of Cu(II) are split by an O_h field into a double degenerate ^2E_g and a triply degenerate $^2T_{2g}$ states. A tetragonal distortion splits ^2E_g into $^2B_{1g}(dx^2\text{-}y^2)$ and $^2A_{1g}(dz^2)$, whereas $^2T_{2g}$ into an orbital singlet $^2B_{2g}(dxy)$ and a doublet $^2E_g(dxy, dy,z)$.[115] The tetragonal distortion may lead to shortening or lengthening of the axial Cu-ligand bonds. In the first case the lowest energy level is $^2B_{1g}(dx^2\text{-}y^2)$ and the following relation between *g* values determined from EPR spectra are expected: $g_{\parallel} > g_{\perp} > g_e$. Shortening of the axial Cu-ligand bond corresponds to the $^2A_{1g}(dz^2)$ ground level and EPR spectra are then characterized by $g_{\perp} > g_{\parallel} = g_e$.[116-119] In our case the *g*-values obtained from EPR are $g_{//} = 2.26$ and $g_{\perp} = 2.05$ and this indicates that the ground level would be $dx^2\text{-}y^2$ at the tetragonal approximation. The lowering of symmetry from tetragonal to C_2 leads to transformation of $^2B_{1g}$, $^2A_{1g}$ and $^2B_{2g}$ into ^2A states, and the doublet ^2E_g is splits into two ^2B single states (Figure S30). Moreover, for symmetry as low as C_2 a significant mixing is expected between ^2A states originating from $^2E_g(O_h)$ as well as between ^2B states originating from $^2T_{2g}(O_h)$ (Figure S30). Accordingly, the lowest state is expected to be a mixed $dx^2\text{-}y^2$ and dz^2 state. Based on the above reasoning and the results of *ab initio* calculations (Section 2.9) the following energy level sequence can be proposed for Cu(II) in **1** assuming approximate C_2 symmetry: $^2A_2(dx^2\text{-}y^2 + dz^2) < {}^2A(dz^2 + dx^2\text{-}y^2) < {}^2A(dxy) < {}^2B(dxz + dy,z) < {}^2B(dxz + dy,z)$ (Figure S30).

Accordingly, to the proposed energy levels structure four bands are expected in absorption spectrum of **1**. Deconvolution of the experimental spectrum using four Gaussian functions is presented in the inset in Figure 6. The obtained bands with maxima at 12743, 14441, 17073 and 18056 cm^{-1} correspond to transitions from the ground $^2A_2(dx^2\text{-}y^2 + dz^2)$ level to the $^2A(dz^2 + dx^2\text{-}y^2)$, $^2B(dxz + dy,z)$, $^2B(dxz + dy,z)$ and $^2A(dxy)$ excited levels. The value of *Dq* in the O_h approximation can be estimated as the difference between the average energy of levels arising from $T_{2g}(O_h)$ and $E_g(O_h)$ states. This yields a value of $Dq \sim 1015$ cm^{-1}, which seems to be reasonably acceptable.

An alternative interpretation could assume that the splitting of the levels arising from $E_g(O_h)$ is small. The absorption spectrum was measured starting from 4000 cm^{-1} and no band was observed in the energy range 4000 – 12,000 cm^{-1}. Hence the energy difference between the two lowest levels $^2A(E_g)$ would have to be smaller than 4000 cm^{-1}. Then the bands observed in the absorption spectrum would be associated with transitions to 3 levels arising from $T_{2g}(O_h)$. Figure S31 shows deconvolution of the spectrum into 3 bands obtained according to this assumption based on interpretation II. Matching the calculated and experimental spectrum is slightly worse than in the case of deconvolution into 4 bands in the inset of Figure 6. Assuming this alternative structure of energy levels and that the center of gravity of levels $A(E_g)$ is below 2000 cm^{-1}, then *Dq* can be estimated as ~ 1285 cm^{-1}.

For compound **2** the RT absorption spectrum is practically the same as for compound **1** (Figure S32). Therefore, for the purpose of present analysis we accepted the same energy level structure for compounds **1** and **2**. The determined limiting values of *Dq*, i.e. 1015 and 1285 cm^{-1} were used in SPM analysis (Section 2.10).

2.9 Ab initio approaches

We searched for B3LYP solutions of total spin $S = ½$ of Cu(II) ions of relevance to the magnetic properties. In Table 3 we list Mulliken populations for Cu atom and neighboring N and O atoms based on X-ray structures of compounds **1** and **2**. The results show localization of charge and spin of Cu 3*d* electrons and support modelling of compounds with pseudospin Hamiltonian[120] with value of spin equal to $S = ½$ (Sections IV and V in SI). Results of Mulliken analysis show that on 3*d* orbitals there are 9.295 electrons, close to nominal value of 9. Spin for 3*d* shell is equal to 0.691, leaking mainly to N atoms. Expectation value of operator of total S^2 is equal to 0.7521, close to ideal value of 0.75. Neighboring O atoms are more electrically polarized than nitrogen atoms suggesting more ionic bonds, which is also supported by Loewdin and Mayer analysis[121] (Table S10). The N atoms are more spin polarized than O atoms, suggesting that Cu-N are more covalent bonds. Comparison of charges on N and O atoms between compounds **1** and **2** also allows us to understand how they translate to the magnetic properties. Charges on the chemically equivalent N atoms are essentially the same for **1** and **2**, whereas main differences arise from the O atoms. O7 and O14 atoms are responsible for the structural distortions (Sections 2.3 and 2.10) and slightly lower charges in **1** than in **2**. The biggest difference in charge comes from the coordinated solvent molecules, with MeOH (**1**) translating to lower charge than H_2O (**2**). This comes from the inherent basicity of the molecule *per se*, but also from the H-bonding pattern that differs within the synthesized systems (Section 2.2). Interestingly, for experimental structure of compound **2** we were not able to get the magnetic solution with

Table 3. Results of Mulliken populations for selected atoms (denoted by cif symbols) calculated using B3LYP DFT and CASSCF for compounds **1** and **2**. Charges are in units of |e| and spin in Bohr magnetons.

1	B3LYP		CASSCF		B3LYP		CASSCF		**2**
Atom	Charge	Spin	Charge	Spin	Charge	Spin	Charge	Spin	Atom
Cu1	0.6856	0.6688	1.2939	0.9788	0.3863	-0.014	1.1559	0.9724	Cu1
O7	-0.4239	-0.0002	-0.6731	0.0009	-0.3923	0.0006	-0.6536	0.0008	O7
N9	-0.1682	0.1273	-0.572	0.0045	-0.2259	0.3141	-0.7979	0.0037	N9
O14	-0.4232	0.0001	-0.6628	0.0007	-0.3989	0.0017	-0.6483	0.0008	O14
N2	-0.1406	0.0798	-0.3651	0.0039	-0.1358	0.04	-0.3350	0.0035	N2
N17	-0.1746	0.0762	-0.4903	0.0041	-0.1244	0.0307	-0.3598	0.0038	N17
O1A	-0.3631	0.0347	-0.5597	0.0024	-0.1829	0	-0.3085	0.0025	O1W

spin localized at the Cu center. Cu atom is nonmagnetized with small leakage of charge (+0.3863|e|). This corresponds more closely to $S = 0$ and Cu(I) oxidation state than to Cu(II; $S = ½$). Only after optimization of geometric structure we obtained magnetic state with localized magnetic moment but during the process of geometry optimization the bond between Cu and H_2O is broken and coordination number changes from 6 to 5. This suggest that there might be close-lying energetic states with different valence properties and geometrical structures. Our computations reveal that the reason for the differences in the properties of both compounds **1** and **2** is not solely related to the immediate surroundings of the Cu ions, but with other factors as well. For test computations we have considered variations due to bound water or methanol. Preliminary results show however that it is not the case. Other factors, *e.g.* changes in valence and ionicity with counterions, may be considered as hypothesis in a future study.

We computed excited states using TDDFT with long-range corrected exchange-correlation functional CAM-B3LYP for compound **1**. Energies of standard B3LYP hybrid functional are underestimated with respect to CAM-B3LYP results. For functional CAM-B3LYP we have used three methods: (i) (simplified) Tamm-Dancoff Approximation[122], (ii) (simplified) TDDFT[123] and (iii) full TDA.[124] Mulliken populations are listed in Table S11 for the ground state these values are similar to those calculated using standard DFT, whereas energies of excited states are listed in Table S12. Local charges and spins are almost identical for methods (i) and (ii), but energies of sTDA and TDA (Table S12) are closer to those calculated using multiconfigurational SCF methods.

Since molecules possess the C_1 symmetry the Kohn-Sham orbitals (microstates) in the ground state may be degenerated only due to accidental degeneracy of spin orbitals. We studied one-electron occupancies of microstates contributing to the ground state and B3LYP results show (due to finite electronic smearing) approximate order of KS orbitals with major contribution of atomic 3*d* orbital as follows: the lowest energy microstate is the doubly occupied 3*d*xz and (α spinorbital) 3*d*z^2 with minor admixture of 3*d*x^2-y^2, followed by 3*d*yz and 3*d*xy orbitals. Next is well separated in energy 3*d*x^2-y^2, which is the closest occupied orbital to the Fermi level. First unoccupied orbital is 3*d*z^2 with minor admixture of 3*d*x^2-y^2 (β spinorbital). Occupied (α spinorbital) counterpart of this spinorbital is the 3*d*z^2 lying near 3*d*xz microstate. Electron occupying this orbital gives main contribution to the magnetic moment. Grouping of electrons is similar to that for higher symmetry cubic case for 3d^9 ions, namely the degenerated state t_{2g} (3*d*xy, 3*d*yz, 3*d*xz) is separated from the degenerated state e_g (3*d*x^2-y^2, 3*d*z^2) lying closer to the Fermi level. The real 3*d* orbitals are expressed in the Cartesian molecular axis system (CMAS) defined in Section IV in SI.

All 4 excited states within the ground multiplet ^{2}D of Cu(II; 3d^9) ion originate from excitations of electron density from occupied orbitals to only one β unoccupied orbital closest to Fermi level (number 167b in ORCA output). This microstate has mainly 3*d*z^2 character consistent with DFT results where unpaired electron (lone hole) in the ground state is of such symmetry. First excited state results mainly from excitation of 3*d*x^2-y^2 electron to 167b state, so we could approximate such state with hole on 3*d*x^2-y^2 orbital. Second and third excited states result from excitation of electron from *d*xy and 3*d*yz orbitals, fourth from 3*d*xz, 3*d*yz and 3*d*xy orbitals. Since TDDFT excited states are due to the *d*-electron excitations similarly as in the crystal field (CF) picture, we assume that such TDDFT states correspond to the CF states. This is confirmed by calculations using CASSCF methods (see below).

To account for dynamic correlations, we performed multiconfigurational-SCF calculations using CASSCF method with additional perturbations NEVPT2. For Cu(II) ion we choose the active space consisting of five orbitals with major contribution of 3*d* atomic states with 9 electrons that could occupy them. Self-convergence procedure leads to five states well separated from each other in energy scale, i.e. orbital singlets (Table 4). Calculations for compound **1** show that the ground state consists of total 9 3*d* electrons in two major configurations: (i) with unpaired 3*d*z^2 electron (~70%) and (ii) with unpaired 3*d*x^2-y^2 electron (~29%). The 1-st excited state is similar to the ground state but proportions are nearly inverted for (ii) with unpaired 3*d*x^2-y^2 electron (~68%) and (i) with unpaired 3*d*z^2 electron (~29%). Other excited states correspond to the following configurations: 2-nd - with unpaired 3*d*xz electron, 3-rd - with unpaired 3*d*xy electron, and 4-th - with unpaired 3*d*yz electron. This is consistent with level schemes for low symmetries from literature[125] and with our semiempirical results and partially also TDDFT.

Calculations for compound **2** show that the ground state consists of total 9 3*d* electrons in two major configurations: (i) with unpaired 3*d*z^2 electron (~77%) and (ii) with unpaired 3*d*x^2-y^2 electron (~22%). The 1st excited state consists of two configurations: (i) with unpaired 3*d*xz electron (~51%) and (ii) with unpaired electron 3*d*x^2-y^2 (~39%). The 2nd excited state is similar to the 1st excited state but proportions are different for (ii) with unpaired 3*d*x^2-y^2 electron (~37%) and (i) with unpaired 3*d*xz electron (~42%). Other excited states correspond to the following configurations: 3rd - with unpaired 3*d*yz electron and 4th - with unpaired 3*d*xy electron. The 3rd and 4th excited state are well separated, suggesting that structure 2 is geometrically

Table 4. Energies of the excited states w.r.t. the ground state (in cm^{-1}) calculated using CASSCF and NEVPT2 for compound **1** and **2**.

Excited state	CASSCF **1**	NEVPT2 **1**	CAM-B3LYP TDA **1**	CASSCF **2**	NEVPT2 **2**
1st	9699	12680	12574	9972	12282
2nd	10420	14255	17761	10547	14048
3rd	12212	16186	17907	12134	16421
4th	12262	16215	18578	13228	18030

more distorted than structure **1**. This would mean that it is associated with the solvent-dependent plane (N2-N9-N17-H_2O) as observed in Section 2.3 (S-value **2** = 0.308 vs S-value **1** = 0.077) and can be directly related to the observed magnetism differences and the literature examples of porphyrins/phthalocyanines, which facilitate SIM/qubit behavior for symmetry reasons.[72, 86-90]

The inclusion of NEVPT2 dynamic corrections for compound **1** shifts the 1st excited state ~3000 cm^{-1} up from the ground state, and ~4000 cm^{-1} for the 2nd, 3rd and 4th exited states. Difference between the 1st excited state and 2nd excited state is enlarged from ~700 cm^{-1} to ~1600 cm^{-1}. Differences between the higher excited states obtained by CASSCF and NEVPT2 are similar. This suggests that dynamical correlations are most relevant for the two lowest states with the unpaired $3dx^2$-y^2 and $3dz^2$ electrons contributing to the magnetic moment. Because accurate description of electronic correlations is crucial for optical spectra, the *ab initio* results are next mapped on effective models to allow comparison with CF energy levels and semiempirical results in Sections 2.8 and 2.10 respectively.

The MC-SCF Mulliken occupations of the selected atoms show some difference with respect to DFT results. Most important is the fact that the spin is more strongly localized at Cu site and electronic charge is closer to nominal charge 2+ (Table 3). Charges on atoms neighboring with Cu are larger than those from DFT. Spins on these neighboring atoms are very small. This is also supported by Loewdin analysis (Table S13). Nonrelativistic CASSCF excited states are well separated from the ground state (GS) and this separation is significantly enlarged with inclusion of dynamic correlations at NEVPT2 level.

Due to such large separations, the mixing of states by SOC is small. The Kramers doublet states resulting from action of SOC (Table 5) indicate that the relative energies are slightly changed with exception of 3rd and 4th excited states, which are now clearly separated in energy, while each being a Kramers doublet, as expected for S = ½. We have listed compositions of wavefunctions for one chosen state from each Kramers doublet

Table 5. Energies of Kramers doublet (KD) states (in cm^{-1}) for compounds **1** and **2**.

KD number	CASSCF **1**	NEVPT2 **1**	CASSCF **2**	NEVPT2 **2**
0 (GS)	0	0	0	0
1	9486	12515	9821	12196
2	10355	14170	10436	13959
3	12157	16071	12332	16566
4	13013	16893	13690	18353

Table 6. The *g*-tensor components for compounds **1** and **2** in the principal axis system (PAS) using ZORA approach.

g-tensor	CASSCF **1**	NEVPT2 **1**	CASSCF **2**	NEVPT2 **2**	B3LYP DFT **1**
g_x	2.081	2.067	2.074	2.058	2.048
g_y	2.115	2.093	2.113	2.087	2.054
g_z	2.517	2.386	2.511	2.409	2.177

for compounds **1** and **2** in Table S14. Such states consist of two components: $|S, +M_S\rangle$ and $|S, -M_S\rangle$ with respective mixing coefficients. Second states from each Kramers doublet have mixing coefficients interchanged for the components $|S, +M_S\rangle$ and $|S, -M_S\rangle$. In the case of compound **1** three lowest KD states consist mainly of one chosen spin free state (i.e. root) with arbitrary spin direction with minor addition of the second spin free state with spin of opposite direction. The fourth and fifth KD states are mixtures of spin free states originating from two roots, which are the 3rd and 4th excited NEVPT2 states. This is not surprising since the 3rd and 4th excited NEVPT2 states are relatively closer in energy and SOC mixes them more strongly. For compound **2** since all NEVPT2 spin free states are well separated, KD states are only mixtures of states originating from one root.

We have calculated the ***g***-tensor components (g_x, g_y, g_z) in the principal axis system (PAS) using ZORA approach (Table 6, Table S15). Results indicate large difference between g_z and (g_x, g_y), whereas g_x and g_y differ slightly since our system has C_1 symmetry. The main magnetic axes, which correspond to the PAS of Zeeman Hamiltonian[126], do not exactly correspond to the molecular bonds of Cu and neighboring atoms but are lying closely. CASSCF method overestimate the ***g***-factors with respect to NEVPT2 method, so (g_i) components derived from the latter one conform well to experimental data for axial symmetry Cu(II) systems.[119, 127-129] We have also listed B3LYP results with the basis aug-cc-pVTZ-J and CP(PPP) for Cu atom with extra fineness of the grid to get more accurate values of the ***g*** tensor. Products of magnetic susceptibilities and temperature $\chi T = \partial^2 E/\partial B^2$ for compounds **1** and **2** obtained using NEVPT2 are plotted in Figure S33. Preliminary plots of EPR spectra (Figures S26 and S27 and Section 2.7) obtained using MOLCAS[112] and PHI[106] support the conclusion that hyperfine structure might be important in such simulations.

We have calculated the ***A***-tensor components (A_x, A_y, A_z) in the principal axis system (PAS) using CASSCF and DFT approach. Results are provided in Section V in SI. The free (spherical symmetry) Cu(II; $3d^9$) ion has only one (ground) multiplet ^2D, which splits in octahedral symmetry CF into the lowest orbital doublet ^2E_g and higher orbital triplet $^2T_{2g}$.[125] We associate tentatively the ground state and the 1st excited state in Table 4 as originating from the doublet, whereas the other excited states from the triplet. This sequence depends on the CF strength and the ^2E_g- and $^2T_{2g}$-states may also intertwine. It is also validated by B3LYP one-electron occupancies of microstates (Kohn-Sham orbitals) contributing to the ground state. To estimate roughly the value of the cubic CFP Dq, we

Table 7. Orbital energies (in cm^{-1}) calculated using *ab initio* Ligand Field for compounds **1** and **2**. Orbitals expressed as the real 3*d* functions correspond to respective LF states.

1 3*d*-orbitals:	z^2	x^2-y^2	xz	xy	yz
CASSCF	12263	2564	1841	50	0
NEVPT2	16215	3535	1960	29	0
2 3*d*-orbitals:	z^2	x^2-y^2 + xz	x^2-y^2 + xz	yz	xy
CASSCF	13228	3256	2681	1095	0
NEVPT2	18030	5749	3982	1609	0

averaged energies of NEVPT2 states contributing to ^2E_g and $^2T_{2g}$. Their difference yields approximate value of the cubic CF splitting 10*Dq* as 9213 cm^{-1}, so *Dq* ~ 921.3 cm^{-1}, close to literature data[125] of 1210 cm^{-1}. The estimation of *Dq* from TDA TDDFT yields *Dq* as 1179.5 cm^{-1}, which is closer to literature data and compares well with those determined in Section 2.8.

We have computed *ab initio* Ligand Field (LF) parameters, i.e. the matrix elements of V_{LF} and Racah parameters (A, B, C) as implemented in ORCA.[130, 131] For the chosen active space in CASSCF or NEVPT2 a unitary operation is done to set all roots closest to L_z single-configurational solutions. In single-electron picture these 5 states correspond to the real 3*d* orbitals (or their combinations). Ligand field is understood as effective field acting on single particle. Corresponding orbital energies obtained using CASSCF and NEVPT2 are listed in Table 7. As expected for d^1 or d^9 ions the computed Racah parameters B and C, which involve two-electron integrals, are zero, whereas A = 217937 cm^{-1} and A = 215623 cm^{-1} for compound **1** and **2**, respectively. Analysis of the LF results of NEVPT2 for compound **1** indicates what follows. The energy 16215 cm^{-1} of state with main contribution of 3dz^2 electron is taken as reference energy. Then absolute energy differences between this energy and the excited states energies are: 12680 (3dx^2-y^2), 14255 (3*d*xz), 16186 (3*d*xy), and 16215 (3*d*yz). These energy differences are almost identical to NEVPT2 energies. This approach yields the lowest state as 3dz^2 hole, next state as 3dx^2-y^2, next two states as mixed 3*d*xz and 3*d*yz, and the highest state as 3*d*xy. This assignment of the single-electron orbitals should correspond directly to semiempirical results obtained using SPM/CFP for set C_{2v} upon diagonalization of CF Hamiltonian within the $|L=2, M_L>$ states of ^2D multiplet (Section 2.10). One-electron excitations from the ground state 3dz^2 to the 1st excited state 3dx^2-y^2 correspond to optical transitions between NEVPT2 molecular states, so our MC-SCF spectrum could be well modeled using LF model with single-particle states expressed as 3*d* real orbitals. There is also agreement with TDDFT results, where excitations are mainly due to hopping of 3*d* electrons to the first unoccupied orbital. Additionally, to gain better insight into optical spectroscopy results (Section 2.8), using pure dipole approximation within NEVPT2 and CASSCF, we have calculated wavelengths corresponding to optical transitions of CD and UV spectra. These values are (in nm): (788.6, 701.5, 617.8, 616.7) and (1031, 959.5, 818.8, 815.5), after conversion to [cm^{-1}] yield (12680, 14255, 16186, 16215) and (9699, 10420, 12212, 12262), respectively, which in the first case compare very well with the experimental energy values of the transitions (12743, 14441, 17073, 18056) (Section 2.8).

Table 8. The CFPs in Wybourne notation B_{kq} (in cm^{-1}) calculated using SPM with *Dq* ~ 1285 cm^{-1} and *Dq* ~ 1015 cm^{-1} for set C_{2v}.

	Complex **1**				Complex **2**			
CFPs:	C_{2v}		C_{2v} after OR/ST*		C_{2v}		C_{2v} after OR/ST*	
Dq	1285	1015	1285	1015	1285	1015	1285	1015
B_{20}	15931	12584	-28719	-22685	16017	12651	-26735	-21118
B_{22}	16945	13385	-1283	-1014	15290	12078	-2163	-1708
B_{40}	31528	24889	21424	16913	30963	24443	21239	16767
B_{42}	-8102	-6396	-1712	-1351	-7429	-5864	-1279	-1010
B_{44}	15305	12082	23758	18756	14822	11701	22958	18123

* The standardization transformation defined as S2[141, 145, 147, 148]: (X, Y, Z) → (X, -Z, Y) was applied.

2.10 SPM and MSH analysis

In order to gain initial assessment of the factors g_i we resorted to the simplified MSH formulas derived for Cu(II; d^9, S = ½) in a tetragonally distorted octahedron. In regular situations, when the EPR spectra are axial with equivalent x and y axes and two *g* values, $g_\parallel$ (g_z) and $g_\perp$ (g_x = g_y), the ground state may be the $|dx^2\text{-}y^2>$ or $|dz^2>$. The following formulas were derived assuming the ground state as dx^2-y^2, which applies to elongated octahedral, square pyramidal or square planar geometry:[118, 125]

$$g_\parallel = 2.0023 \pm \frac{8\xi}{E\left(d_{x^2-y^2}\right)-E(d_{xy})} \quad (1)$$

$$g_\perp = 2.0023 \pm \frac{2\xi}{E\left(d_{x^2-y^2}\right)-E(d_{xz})} = 2.0023 \pm \frac{2\xi}{E\left(d_{x^2-y^2}\right)-E(d_{yz})} \quad (2)$$

For Cu(II; d^9, S = ½) complexes the + sign applies in Eqs (1) and (2), so the g_i factors are higher than g_e (= 2.0023). Eqs (1) and (2) include only the spin-orbit coupling (ζ) contributions arising from the second order perturbation theory, which may be not adequate for more realistic predictions. Similar formulas apply for the ground state $|dz^2>$, which is an alternative option for the idealized tetragonal site symmetry of a compressed octahedron. These initial estimates have indicated suitability of the MSH approach (2).

For more accurate calculations of SHPs, we employ the MSH formulas for tetragonal[132-138] and orthorhombic[139-141] symmetry. First, to obtain input data for MSH formulas, the CFPs B_{kq}[142-144] are calculated using SPM for Cu(II) centers in **1** and **2** using the structural data for set C_{2v} (Section IV in SI). The two plausible *Dq* values ~1015 cm^{-1} and ~1285 cm^{-1} estimated by us experimentally from optical spectra (Section 2.8) are adopted. Pertinent comments on reliability of usage of SPM/CFP predictions as input data for MSH formulas are provided in Section VI in SI. The results listed in Table 8 indicate that after standardization (see Section VI in SI) we obtain the axial CFP B_{20} of the highest magnitude and minimal values of B_{22} and B_{42}, while B_{20} and B_{22} also change signs to conform to the

choice of positive rhombicity ratio built into the package CST.[145, 146]

The relations between the CF energy levels in Eqs (1) and (2) and those E_1 and E_2 employed in MSH formulas for tetragonal symmetry in[133, 136] are as follows:

$$E_1 = 10Dq = \Delta E = (|dx^2\text{-}y^2> - |dxy>)$$

$$E_2 = 10Dq - 3Ds + 5Dt = \Delta E = (|dx^2\text{-}y^2> - |dyz>) = \Delta E = (|dx^2\text{-}y^2> - |dxz>) \quad (3)$$

In Eq. (3) Dq denotes the cubic CFP, whereas Ds and Dt denote the second- and fourth-rank tetragonal CFPs in the conventional notation[149, 150], respectively. Depending on the shape of the distorted octahedron (Section 2.3) and thus the strength of tetragonal CFPs, the ground state may be either $|dx^2\text{-}y^2>$ or $|dz^2>$.[118, 125] This is also evident in our ab initio calculations (Section 2.9). Next, using the CFPs in Table 8 and the conversion relations between the CFPs B_{kq} and (Ds, Dt) given in[11, 14, 150], the latter CFPs are calculated, and subsequently, the energies E_1 and E_2 in Eq. (3). Finally, the tetragonal SHPs: g_i and A_i are calculated applying the respective MSH formulas.[133, 136] To calculate the hyperfine structure parameters A_i we employ analogous MSH formulas derived as functions of the g_i values and respective CF energies.[132-138]

For orthorhombic symmetry[139-141], four CF energies E_i (i = 1 – 4) apply. The corresponding relations are:

$$E_1 = 10Dq$$

$$E_2 = 10Dq + 3Ds - 5Dt - 3D_\xi + 4D\eta^2$$

$$E_3 = 10Dq + 3Ds - 5Dt + 3D_\xi - 4D\eta^2$$

$$E_4 = -4Ds - 5Dt \quad (4)$$

In Eq. (4) Dq, Ds and Dt have the same meaning as in Eq. (3), whereas D_ξ and D_η are the conventional orthorhombic CFPs, which are related to the CFPs B_{kq}. The orthorhombic (OR) SHPs g_i and A_i calculated applying the respective MSH formulas[139-141] are listed in Table 9. To facilitate comparison of the orthorhombic g_i and A_i components and the perpendicular tetragonal ones, the averaged values: $(g_x+g_y)/2 \sim g_\perp$ and $(A_x+A_y)/2 \sim A_\perp$ are also calculated, while the axial components are directly comparable: $g_z \sim g_\parallel$ and $A_z \sim A_\parallel$.

A few important points bearing on interpretation of results in Table 9 must be kept in mind.

(i) The numbering (i = 1 – 4) of CF energies (E_i) does not reflect any ordering in magnitude. In Eq. (4), E_4 represents the splitting of the lower orbital E-doublet. The values of E_4 are obtained as negative in our calculations. However, for proper interpretation of the sequence of CF energies (-) sign of E_4 must be changed to (+) sign, since here it only reflects the change of the nominal ground state within the lower orbital E-doublet from one option to another, i.e. either $|dx^2\text{-}y^2>$ or $|dz^2>$. So the negative E_4 sign affects only that the sequence of the states assigned to the first two CF energy levels and indicates that they should be inverted: $|dx^2\text{-}y^2> \leftrightarrow |dz^2>$. It does not mean that the negative value of E_4 should be taken as the ground level and other levels rescaled to such ground level set to zero. This finding bears significantly on interpretation of CF energies obtained from Eq. (4) and proper comparison with optical spectra presented in Section 2.8. Note that for monoclinic C_2 and triclinic C_1 symmetry the ground state becomes an admixture of both states $|dx^2\text{-}y^2>$ and $|dz^2>$ (Sections 2.8 and 2.9). (ii) It should also be noted that by reducing the set of four orthorhombic CF energies E_i (i = 1 – 4) in Eq. (4) to the tetragonal case by setting orthorhombic CFPs to zero, instead of two CF energies E_i (i = 1, 2) in Eq. (3), we obtain three CF energies: E_1, $E_2 = E_3$ and E_4. This mismatch arises from omission in[133, 136, 150] of the third CF energy level E_4, which exists for tetragonal symmetry. This can be checked by reducing orthorhombic equations for g_i and A_i to tetragonal case. Then, it turns out that the CF energy E_4, which represents the splitting of the lower orbital E-doublet for tetragonal symmetry, gives no contributions to g_i and A_i. It appears that for this reason E_4 was simply omitted in MSH formulas in source papers.[132-138] (iii) There is an apparent problem: how to explain that the Dq values in the lower (OR) part of Table 9 differ from those in the upper (TE) part, which are equal to the respective 'input' Dq values? This is due to different formulas adopted in calculations of the cubic CF parameter Dq in the TE and OR case. The Dq values adopted in the TE case are those experimentally determined from optical spectra, which directly correspond to E_1 in Eq. (3), whereas no

Table 9. The conventional CFPs calculated using the CFPs B_{kq} in Table 8 together with energy levels: E_i (all in cm^{-1}) and SHPs: g_i (dimensionless) and A_i (in 10^{-4} cm^{-1}).

	TE formulas adopted							
	Complex **1**				Complex **2**			
	C_{2v}		C_{2v} after OR/ST		C_{2v}		C_{2v} after OR/ST	
Dq	1285	1015	1285	1015	1285	1015	1285	1015
Ds	-2276	-1798	4103	3241	-2288	-1807	3819	3017
Dt	-282	-222	873	689	-293	-232	818	646
E_1	12850	10150	12850	10150	12850	10150	12850	10150
E_2	7431	5869	20794	16427	7452	5886	20218	15972
$g_\perp$	2.1168	2.1469	2.0499	2.0646	2.1165	2.1464	2.0510	2.0659
$g_\parallel$	2.2879	2.3699	2.2713	2.3432	2.2879	2.3697	2.2715	2.3435
$A_\perp$	16.1	22.9	0.9	4.2	16.0	22.8	1.1	4.5
$A_\parallel$	-171.9	-152.0	-168.4	-149.5	-171.9	-152.0	-168.5	-149.6
	OR formulas adopted							
Dq	1220	963	1893	1495	1181	932	1829	1444
Ds	-2276	-1798	4103	3241	-2288	-1807	3819	3017
Dt	-282	-222	873	689	-293	-232	818	646
$D\zeta$	1977	1561	-150	-118	1783	1409	-252	-199
$D\eta$	610	482	129	102	559	442	96	76
E_1	12195	9627	18931	14945	11810	9324	18293	14441
E_2	3287	2589	27839	21983	3300	2599	26804	21165
E_3	10266	8104	25910	20460	9526	7520	24519	19361
E_4	10512	8303	20775	16409	10619	8387	19367	15296
g_x	2.2423	2.3003	2.0358	2.0455	2.2420	2.2997	2.0371	2.0473
g_y	2.1008	2.1342	2.0382	2.0487	2.1063	2.1406	2.0403	2.0514
$(g_x+g_y)/2$	2.1716	2.2173	2.0370	2.0471	2.1742	2.2202	2.0387	2.0494
g_z	2.3236	2.4232	2.1852	2.2341	2.3343	2.4372	2.1916	2.2425
A_x	140.1	154.7	84.2	86.4	139.6	154.2	84.5	86.8
A_y	-83.0	-76.9	-88.3	-85.9	-81.4	-75.0	-87.8	-85.2
$(A_x+A_y)/2$	28.55	38.9	-2.05	0.25	29.1	39.6	-1.65	0.8
A_z	-126.4	-92.0	-183.1	-167.7	-123.0	-87.6	-181.1	-165.0

specific relation was provided for *Dq* in.[132-138] However, in the OR case *Dq*, i.e. E_1 in Eq. (4), is calculated using the relation:[139-141] $Dq = \sqrt{70/105}\, B_{44}$

The differences between the OR and TE *Dq* values amount up to about 30% for set C_{2v} after OR/ST, whereas only 5% for set C_{2v}. Analysis of the results in Table 9 lead to the following conclusions. The SHPs g_i and A_i calculated using MSH formulas for the tetragonal (TE) case may be directly compared with experimental results in Section 2.3, whereas those for the orthorhombic (OR) case - with the *ab initio* results in Section 2.9. Results for both cases indicate good mutual consistency, which shows the usefulness of the ascent/descent in symmetry.[151-153] Employing the standardized CFP sets in MSH calculations is even more crucial in the TE case than in the OR case, in view of additional approximations involved in the TE case, i.e. omitting the orthorhombic CFPs: B_{22} and B_{42}.

The values of g_i calculated in Table 9 by adopting TE and OR formulas agree well with our experimental ones: $g_{\|}$ = 2.26 and $g_{\perp}$ = 2.05 for complex **1** and also with literature data obtained for compounds with axial symmetry Cu-sites, see Table 10. Since EPR spectra were done on powdered samples, the axes (x, y, z) implicitly involved in experimental values: $g_{\|}$ (z), $g_{\perp}$ (x, y) may be considered only as *nominal* principal axes. To relate the axes (x, y, z) directly to the crystal structure, e.g. to find out if the z-axis corresponds to the orientations of the long axis of the coordination octahedron (Figures 1c,d), EPR measurements on powdered microcrystalline samples would be required. Comparison of the theoretical A_i values in Table 9 with our experimental value $A_{||}$ = 175 (G) = 165.8 (10^{-4} cm^{-1}) for complex **1** and the respective values in Table 10 reveals that all experimental $A_{\|}$ are positive, whereas theoretical ones are negative. This is due to the limited capabilities of the computer program used, have allowed fitting EPR spectra only with the absolute values of the hyperfine interaction parameters $|A|$. Since no perpendicular splitting has been observed in EPR spectrum, no accurate value of $A_{\perp}$ could be determined. Attempts to simulate spectra using $A_{\perp}$ indicate that this is not a sensitive parameter because any splitting is hidden in the main EPR line. A good match has been obtained with $A_{\perp}$ equal 1 as well as 20 cm^{-1}. Both formulas: TE and OR ones, yield comparable sets of results and indicate that good agreements may be obtained by appropriate matching of the adjustable parameters. However, overall the *Dq* value (in cm^{-1}) 1015 seems better 1285, which yields larger CF energies (E_i). This finding conforms to that obtained in Section 2.8. Comparison of the TE and OR results for sets C_{2v} or both complexes **1** and **2** in Table 9 indicates smaller differences between the respective results than those for sets C_{2v} after OR/ST. This may be due to the approximations involved in the TE case. Since no such approximations are involved in the OR case, the results for sets C_{2v} after OR/ST may be considered as more accurate. Comparison of the results in Table 9 and the respective results obtained by *ab initio* methods (Section 2.9) also favor the MSH results obtained with lower *Dq* value for sets C_{2v} after OR/ST. Importantly, the CF energies obtained for sets C_{2v} do not agree as well those for sets C_{2v} after OR/ST. This reinforces the importance of employing orthorhombic standardization.

Diagonalization[154, 155] of the CF Hamiltonian H_{CF} using the correspondence between spin S = 2 states and spin L = 2 states is anticipated in the future studies. Calculations of the CF energy levels and composition of the $|L=2, M_L\rangle = |M_L\rangle$ states will enable assessment of their dominant contributions and thus verification if the semiempirically predicted ground state conforms to that obtained by optical spectroscopy and *ab initio* methods. In order to allow a better correlation of overall results, an attempt will be made to fit raw EPR data using orthorhombic g_i and A_i components as well.

Table 10. The axial g_i factors (dimensionless) and hyperfine A_i parameters (in 10^{-4} cm^{-1}) reported for Cu(II) ions in various compounds.

Compound	$g_{\|}$	$g_{\perp}$	$A_{\|\|}$	$A_{\perp}$	Ref.	10*Dq*
CaB_4O_7: CuO	2.32	2.06	146.4 [154.5]*	27.0 [28.5]	Expt. [127]	
	2.32	2.06	-154	-28	Theo.[133]	13330
$LiRbB_4O_7$: CuO	2.4451	2.0561	158	-	Expt. [129]	
	2.445	2.058	-166	-22	Theo.[134]	
$[CuL_2]$ 2MeOH[&]	2.260	2.050	158.2 [167]*#	-	Expt. [85]	

* The original Ai values in units of [Gauss] were converted to [cm^{-1}] using relation: P [Gauss] => g x 0.4669 x P [10^{-4} cm^{-1}], where g is the spectroscopic splitting factor. [&] L – deprotonated form of 2-methoxy-6-(E-2-pyridyliminomethyl)-phenol. [#] No units were assigned for the value 167 but since EPR spectra were in [G], we assumed [G] for $A_{\|}$.

3. Conclusions

We prepared a modular system for general studies on how subtle structural differences can affect magnetic relaxation properties in transition metal coordination compounds. Tunable character of synthesized complexes comes from: (i) novel pentadentate $\mathbf{L^{red\text{-}R}}$ *N,O*-aminal ligand formed by unexpected *in situ* reduction of the parent Schiff base ligand **L**; (ii) the chosen solvent/reagent alcohol; (iii) coordination preferences of metal salt and its counterion. Considering that the SIM-active d^9 coordination compounds are rarely encountered, two structurally similar octahedral Cu(II) compounds were prepared as the case study. Both analogues were revealed to be rare examples of magnetically isolated copper system that display slow relaxation of magnetisation, with phenomenon being more pronounced for the perchlorate analogue **1** than the triflate **2**.[23] Extensive series of experimental and theoretical techniques allowed us to understand the effect of geometrical and structural changes on copper(II) electronic states and consequently observed magnetic behaviour. It is predominantly the result of the octahedral structural distortions exerted by the alkoxy groups appended on the $\mathbf{L^{red\text{-}R}}$ scaffold. Elongation along the (O7···O14) direction translates to the hyperfine structure observed in the EPR spectra, plausibly related to the interactions of Cu(II) ion with the nuclear spin I = $^3/_2$. This renders the system more square planar character within the ligand-solvent plane and slow magnetic relaxation phenomenon is observed despite the inherently detrimental character of the nitrogen atoms.[91] Relaxation of magnetization would therefore proceed through the four Raman allowed

transitions ($\Delta M_S = \pm 1$, $\Delta M_I = 0$) since the Orbach process is not applicable to the $S = ½$ systems.[156]

To gain further understanding of the magnetic studies, an extensive series of *ab initio* ((TD-)DFT, CASSCF, NEVPT2) and semiempirical (SPM, MSH) calculations was also conducted. Cu(II) electronic states, *g*-tensor and *A*-tensor components as well as ligand field parameters were calculated and compared with the experimentally determined values. Specifically, such thorough and complementary utilization of these techniques for Cu(II) states was performed for the first time, which will delineate possibilities and limitations of these approaches in the future. In addition, the close-lying energetic states of Cu(I)/Cu(II) possibly influence much faster relaxation in **2**, which shows that factors other than structural distortions also need also to be accounted for the design of Cu(II)-based SIMs/qubits. We anticipate that results of this study will facilitate rational design of the synthesis and thus in-depth characterization of new Cu(II) SIMs/qubits in the future. Specifically, presented modular platform can be further utilized for magneto-structural correlations in other magnetic systems, which we are currently investigating further.

Associated content

Author Information

Corresponding Authors

Adam Gorczyński - [a]*Faculty of Chemistry, Adam Mickiewicz University, Uniwersytetu Poznańskiego 8, 61-614 Poznań, Poland; Email: adam.gorczynski@amu.edu.pl; ORCID: 0000-0002-3930-8489*

Maria Korabik - [e]*Faculty of Chemistry, University of Wrocław, F. Joliot-Curie 14, 50-383 Wrocław, Poland; Email: maria.korabik@chem.uni.wroc.pl; ORCID:* 0000-0002-9970-9743

Authors

Dawid Marcinkowski - [a]Faculty of Chemistry, Adam Mickiewicz University, Uniwersytetu Poznańskiego 8, 61-614 Poznań, Poland; *ORCID: 0000-0001-6053-3229*

Ariel Adamski - [a]*Faculty of Chemistry, Adam Mickiewicz University, Uniwersytetu Poznańskiego 8, 61-614 Poznań, Poland; ORCID: 0000-0003-3205-6968*

Maciej Kubicki - [a]*Faculty of Chemistry, Adam Mickiewicz University, Uniwersytetu Poznańskiego 8, 61-614 Poznań, Poland; ORCID: 0000-0001-7202-9169*

Giuseppe Consiglio - [b]*Dipartimento di Scienze Chimiche, Università di Catania, I-95125 Catania, Italy; ORCID: 0000-0002-2682-269X*

Violetta Patroniak - [a]*Faculty of Chemistry, Adam Mickiewicz University, Uniwersytetu Poznańskiego 8, 61-614 Poznań, Poland; ORCID 0000-0001-9976-7233*

Tomasz Ślusarski - [a]*Faculty of Chemistry, Adam Mickiewicz University, Uniwersytetu Poznańskiego 8, 61-614 Poznań, Poland; [c]Institute of Spintronics and Quantum Information, Faculty of Physics, Adam Mickiewicz University, Uniwersytetu Poznańskiego 2, 61-614 Poznań, Poland; ORCID: 0000-0003-3269-1558*

Muhammed Açıkgöz - [d]*Department of Science, The State University of New York (SUNY) Maritime College, New York 10465, USA; ORCID: 0000-0003-4165-0854*

Daria Szeliga - [e]*Faculty of Chemistry, University of Wrocław, F. Joliot-Curie 14, 50-383 Wrocław, Poland; ORCID: 0000-0001-7656-3107*

Nahir Vadra - [a]*Faculty of Chemistry, Adam Mickiewicz University, Uniwersytetu Poznańskiego 8, 61-614 Poznań, Poland;* [f]*Universidad de Buenos Aires, Facultad de Ciencias Exactas y Naturales, Departamento de Química Inorgánica, Analítica y Química Física and CONICET–Universidad de Buenos Aires, Instituto de Química Física de los Materiales, Medio Ambiente y Energía (INQUIMAE), Buenos Aires C1428EGA, Argentina; ORCID: 0000-0001-5652-926X*

Mirosław Karbowiak - [e]*Faculty of Chemistry, University of Wrocław, F. Joliot-Curie 14, 50-383 Wrocław, Poland; ORCID: 0000-0001-7077-8481*

Ireneusz Stefaniuk - [g]*College of Natural Sciences, University of Rzeszow, Rejtana 16a, 35-310 Rzeszow, Poland; ORCID: 0000-0003-2616-9595*

Czesław Rudowicz - [a]*Faculty of Chemistry, Adam Mickiewicz University, Uniwersytetu Poznańskiego 8, 61-614 Poznań, Poland; ORCID: 0000-0003-0370-9392*

CRediT authorship contribution statement

Dawid Marcinkowski: Synthesis of chemical compounds, magneto-structural correlations: Conceptualization, Methodology, Formal analysis, Investigation, Resources, Data curation, Writing - original draft, Writing - review & editing, Visualization.
Ariel Adamski: Synthesis of chemical compounds: Conceptualization, Methodology, Formal analysis, Investigation, Resources, Data curation, Writing - review & editing, Visualization.
Maciej Kubicki: Crystallographic studies: Formal analysis, Investigation, Data curation, Writing - review & editing, Visualization.
Giuseppe Consiglio: Synthesis of compounds: Formal analysis, Investigation, Data curation, Writing - review & editing.
Violetta Patroniak: Methodology, Formal analysis, Investigation, Writing - review & editing, Supervision.
Tomasz Ślusarski: Theoretical studies: Formal analysis, Investigation, Data curation, Writing - review & editing, Visualization.
Muhammed Açıkgöz: Theoretical studies: Formal analysis, Investigation, Data curation, Writing - review & editing, Visualization.
Daria Szeliga: DC/AC magnetism studies: Formal analysis, Investigation, Data curation, Writing - review & editing, Visualization.
Nahir Vadra: Magneto-structural correlations: Data curation, Writing - review & editing, Visualization.

Mirosław Karbowiak: Spectroscopic and theoretical studies: Conceptualization, Methodology, Formal analysis, Investigation, Resources, Data curation, Writing - review & editing, Visualization.
Ireneusz Stefaniuk: EPR studies: Conceptualization, Methodology, Formal analysis, Investigation, Resources, Data curation, Writing - review & editing, Visualization.
Czesław Rudowicz: Magneto-structural correlations, SPM and MSH analysis: Conceptualization, Methodology, Formal analysis, Investigation, Resources, Data curation, Writing - review & editing, Visualization, Supervision, Funding acquisition.
Adam Gorczyński: Magneto-structural analysis and correlations: Conceptualization, Methodology, Formal analysis, Investigation, Resources, Data curation, Writing - original draft, Writing - review & editing, Visualization, Supervision.
Maria Korabik: DC/AC magnetism studies, EPR studies: Conceptualization, Methodology, Formal analysis, Investigation, Resources, Data curation, Writing - review & editing, Visualization, Supervision.

Conflicts of interest

There are no conflicts to declare.

Acknowledgements

This work was mainly supported by: (PI: CZR): UMO-2016/21/B/ST4/02064 from the Polish National Science Center and partially from the budget for science in 2018-2020, as a part of the Polish Ministry of Science and Higher Education project; (PI: DM): Grant No. 0088/DIA/2018/47 in the frame of the "Diamond Grant" programme; (PI: AG): SONATA grant UMO-2020/39/D/ST4/01182 from National Science Centre, Poland. The calculations were made at the Poznań Supercomputing and Networking Center. Technical assistance with impulse EPR measurements from M.Sc. B. Cieniek is much appreciated

References

1. E. Coronado, *Nat. Rev. Mater*, 2019, DOI: 10.1038/s41578-019-0146-8.
2. C. A. P. Goodwin, *Dalton Trans.*, 2020, **49**, 14320-14337.
3. A. Zabala-Lekuona, J. M. Seco and E. Colacio, *Coord. Chem. Rev.*, 2021, **441**, 213984.
4. C. E. Jackson, I. P. Moseley, R. Martinez, S. Sung and J. M. Zadrozny, *Chem. Soc. Rev.*, 2021, **50**, 6684-6699.
5. R. Mirzoyan, N. P. Kazmierczak and R. G. Hadt, *Chem. Eur. J.*, 2021, **27**, 9482-9494.
6. M. S. Fataftah and D. E. Freedman, *Chem. Commun.*, 2018, **54**, 13773-13781.
7. M. Affronte, *J. Mater. Chem.*, 2009, **19**, 1731-1737.
8. E. Moreno-Pineda and W. Wernsdorfer, *Nat. Rev. Phys.*, 2021, DOI: 10.1038/s42254-021-00340-3.
9. K. Head-Marsden, J. Flick, C. J. Ciccarino and P. Narang, *Chem. Rev.*, 2021, **121**, 3061-3120.
10. K. S. Pedersen, A.-M. Ariciu, S. McAdams, H. Weihe, J. Bendix, F. Tuna and S. Piligkos, *J. Am. Chem. Soc.*, 2016, **138**, 5801-5804.
11. A. Gaita-Ariño, H. Prima-García, S. Cardona-Serra, L. Escalera-Moreno, L. E. Rosaleny and J. J. Baldoví, *Inorg. Chem. Front.*, 2016, **3**, 568-577.
12. M. Atzori and R. Sessoli, *J. Am. Chem. Soc.* , 2019, **141**, 11339-11352.
13. A. Gaita-Ariño, F. Luis, S. Hill and E. Coronado, *Nat. Chem.*, 2019, **11**, 301-309.
14. C.-J. Yu, S. von Kugelgen, D. W. Laorenza and D. E. Freedman, *ACS Cent. Sci.*, 2021, **7**, 712-723.
15. S. E. Crawford, R. A. Shugayev, H. P. Paudel, P. Lu, M. Syamlal, P. R. Ohodnicki, B. Chorpening, R. Gentry and Y. Duan, *Adv. Quantum Technol.*, 2021, **4**, 2100049.
16. S. Krastanov, M. Heuck, J. H. Shapiro, P. Narang, D. R. Englund and K. Jacobs, *Nat. Commun.*, 2021, **12**, 191.
17. R. S. D. Gatteschi, J. Villain, *Molecular Nanomagnets*, Oxford University Press, Oxford, 2006.
18. F. L. J. Bartolomé, J.F. Fernández, *Molecular Nanomagnets: Physics and Applications*, Springer-Verlag Berlin, Heidelberg, 2014.
19. D. G. C. Benelli, *Introduction to Molecular Magnetism: From Transition Metals to Lanthanides*, Wiley-VCH, Weinheim 2015.
20. M. M. R.A. Layfield, *Lanthanides and Actinides in Molecular Magnetism*, Wiley-VCH, Weinheim 2015.
21. P. Z. J. Tang, *Lanthanide Single Molecule Magnets*, Springer-Verlag Berlin Heidelberg, 2015.
22. E. S. Gao, *Molecular Nanomagnets and Related Phenomena, Structure and Bonding*, Springer-Verlag Berlin, Heidelberg, 2015.
23. R. Boča and C. Rajnák, *Coord. Chem. Rev.*, 2021, **430**, 213657.
24. C. Rajnák and R. Boča, *Coord. Chem. Rev.*, 2021, **436**, 213808.
25. D. Shao and X.-Y. Wang, *Chin. J. Chem.*, 2020, **38**, 1005-1018.
26. R. Marin, G. Brunet and M. Murugesu, *Angew. Chem. Int. Ed.*, 2021, **60**, 1728-1746.
27. V. S. Parmar, D. P. Mills and R. E. P. Winpenny, *Chem. Eur. J.*, 2021, **27**, 7625-7645.
28. T. Lis, *Acta Cryst. B*, 1980, **36**, 2042-2046.
29. R. Sessoli, D. Gatteschi, A. Caneschi and M. A. Novak, *Nature*, 1993, **365**, 141-143.
30. K. S. Pedersen, J. Bendix and R. Clérac, *Chem. Comm.*, 2014, **50**, 4396-4415.
31. D. N. Woodruff, R. E. P. Winpenny and R. A. Layfield, *Chem. Rev.*, 2013, **113**, 5110-5148.
32. J.-L. Liu, Y.-C. Chen and M.-L. Tong, *Chem. Soc. Rev.*, 2018, **47**, 2431-2453.
33. S. Gómez-Coca, D. Aravena, R. Morales and E. Ruiz, *Coord. Chem. Rev.*, 2015, **289-290**, 379-392.
34. A. B. Canaj, S. Dey, E. R. Martí, C. Wilson, G. Rajaraman and M. Murrie, *Angew. Chem. Int. Ed.*, 2019, **58**, 14146-14151.
35. Y.-S. Ding, N. F. Chilton, R. E. P. Winpenny and Y.-Z. Zheng, *Angew. Chem. Int. Ed.*, 2016, **55**, 16071-16074.
36. Z.-H. Li, Y.-Q. Zhai, W.-P. Chen, Y.-S. Ding and Y.-Z. Zheng, *Chem. Eur. J.*, 2019, **25**, 16219-16224.
37. J. M. Frost, K. L. M. Harriman and M. Murugesu, *Chem. Sci.*, 2016, **7**, 2470-2491.

38. G. A. Craig and M. Murrie, *Chem. Soc. Rev.*, 2015, **44**, 2135-2147.
39. F.-S. Guo, B. M. Day, Y.-C. Chen, M.-L. Tong, A. Mansikkamäki and R. A. Layfield, *Sci.*, 2018, **362**, 1400.
40. C. A. P. Goodwin, F. Ortu, D. Reta, N. F. Chilton and D. P. Mills, *Nature*, 2017, **548**, 439-442.
41. F.-S. Guo, B. M. Day, Y.-C. Chen, M.-L. Tong, A. Mansikkamäki and R. A. Layfield, *Angew. Chem. Int. Ed.*, 2017, **56**, 11445-11449.
42. K. Randall McClain, C. A. Gould, K. Chakarawet, S. J. Teat, T. J. Groshens, J. R. Long and B. G. Harvey, *Chem. Sci.*, 2018, **9**, 8492-8503.
43. M. J. Giansiracusa, A. K. Kostopoulos, D. Collison, R. E. P. Winpenny and N. F. Chilton, *Chem. Comm.*, 2019, **55**, 7025-7028.
44. S. E. Stavretis, D. H. Moseley, F. Fei, H.-H. Cui, Y. Cheng, A. A. Podlesnyak, X. Wang, L. L. Daemen, C. M. Hoffmann, M. Ozerov, Z. Lu, K. Thirunavukkuarasu, D. Smirnov, T. Chang, Y.-S. Chen, A. J. Ramirez-Cuesta, X.-T. Chen and Z.-L. Xue, *Chem. Eur. J.*, 2019, **25**, 15846-15857.
45. B. Yin and C.-C. Li, *Phys. Chem. Chem. Phys.*, 2020, **22**, 9923-9933.
46. A. Castro-Alvarez, Y. Gil, L. Llanos and D. Aravena, *Inorg. Chem. Front.*, 2020, **7**, 2478-2486.
47. Y.-Q. Zhai and Y.-Z. Zheng, *J. Mat. Chem. C*, 2021, **9**, 8096-8098.
48. L. Escalera-Moreno, J. J. Baldoví, A. Gaita-Ariño and E. Coronado, *Chem. Sci.*, 2018, **9**, 3265-3275.
49. E. Bartolomé, A. Arauzo, J. Luzón, J. Bartolomé and F. Bartolomé, in *Handbook of Magnetic Materials*, ed. E. Brück, Elsevier, 2017, vol. 26, pp. 1-289.
50. S. Karasawa, G. Zhou, H. Morikawa and N. Koga, *J. Am. Chem. Soc.*, 2003, **125**, 13676-13677.
51. W. H. Harman, T. D. Harris, D. E. Freedman, H. Fong, A. Chang, J. D. Rinehart, A. Ozarowski, M. T. Sougrati, F. Grandjean, G. J. Long, J. R. Long and C. J. Chang, *J. Am. Chem. Soc.*, 2010, **132**, 18115-18126.
52. X. N. Yao, J. Z. Du, Y. Q. Zhang, X. B. Leng, M. W. Yang, S. D. Jiang, Z. X. Wang, Z. W. Ouyang, L. Deng, B. W. Wang and S. Gao, *J. Am. Chem. Soc.*, 2017, **139**, 373-380.
53. J. Vallejo, I. Castro, R. Ruiz-García, J. Cano, M. Julve, F. Lloret, G. De Munno, W. Wernsdorfer and E. Pardo, *J. Am. Chem. Soc.*, 2012, **134**, 15704-15707.
54. R. Mitsuhashi, K. S. Pedersen, T. Ueda, T. Suzuki, J. Bendix and M. Mikuriya, *Chem. Comm.*, 2018, **54**, 8869-8872.
55. O. Stetsiuk, A. El-Ghayoury, F. Lloret, M. Julve and N. Avarvari, *Eur. J. Inorg. Chem.*, 2018, **2018**, 449-457.
56. P. C. Bunting, M. Atanasov, E. Damgaard-Møller, M. Perfetti, I. Crassee, M. Orlita, J. Overgaard, J. van Slageren, F. Neese and J. R. Long, *Science*, 2018, **362**, eaat7319.
57. J. M. Zadrozny, D. J. Xiao, M. Atanasov, G. J. Long, F. Grandjean, F. Neese and J. R. Long, *Nat. Chem.*, 2013, **5**, 577-581.
58. D. E. Freedman, W. H. Harman, T. D. Harris, G. J. Long, C. J. Chang and J. R. Long, *J. Am. Chem. Soc.*, 2010, **132**, 1224-1225.
59. P. P. Samuel, K. C. Mondal, N. Amin Sk, H. W. Roesky, E. Carl, R. Neufeld, D. Stalke, S. Demeshko, F. Meyer, L. Ungur, L. F. Chibotaru, J. Christian, V. Ramachandran, J. Van Tol and N. S. Dalal, *J. Am. Chem. Soc.*, 2014, **136**, 11964-11971.
60. Y. S. Meng, Z. Ouyang, M. W. Yang, Y. Q. Zhang, L. Deng, B. W. Wang and S. Gao, *Inorg. Chem. Front.*, 2019, **6**, 1050-1057.
61. C. J. Milios and R. E. P. Winpenny, in *Molecular Nanomagnets and Related Phenomena*, ed. S. Gao, Springer Berlin Heidelberg, Berlin, Heidelberg, 2015, DOI: 10.1007/430_2014_149, pp. 34-56.
62. R. C. Poulten, M. J. Page, A. G. Algarra, J. J. Le Roy, I. López, E. Carter, A. Llobet, S. A. Macgregor, M. F. Mahon, D. M. Murphy, M. Murugesu and M. K. Whittlesey, *J. Am. Chem. Soc.*, 2013, **135**, 13640-13643.
63. W. Lin, T. Bodenstein, V. Mereacre, K. Fink and A. Eichhöfer, *Inorg. Chem.* , 2016, **55**, 2091-2100.
64. J. Miklovič, D. Valigura, R. Boča and J. Titiš, *Dalton Trans.*, 2015, **44**, 12484-12487.
65. I. Bhowmick, A. J. Roehl, J. R. Neilson, A. K. Rappé and M. P. Shores, *Chem. Sci.*, 2018, **9**, 6564-6571.
66. H.-H. Cui, J. Wang, X.-T. Chen and Z.-L. Xue, *Chem. Comm.*, 2017, **53**, 9304-9307.
67. L. Chen, J. Song, W. Zhao, G. Yi, Z. Zhou, A. Yuan, Y. Song, Z. Wang and Z.-W. Ouyang, *Dalton Trans.*, 2018, **47**, 16596-16602.
68. J. J. Scepaniak, C. S. Vogel, M. M. Khusniyarov, F. W. Heinemann, K. Meyer and J. M. Smith, *Science*, 2011, **331**, 1049.
69. M. Ding, G. E. Cutsail Iii, D. Aravena, M. Amoza, M. Rouzières, P. Dechambenoit, Y. Losovyj, M. Pink, E. Ruiz, R. Clérac and J. M. Smith, *Chem. Sci.*, 2016, **7**, 6132-6140.
70. G. E. Cutsail Iii, B. W. Stein, D. Subedi, J. M. Smith, M. L. Kirk and B. M. Hoffman, *J. Am. Chem. Soc.*, 2014, **136**, 12323-12336.
71. F. Liedy, J. Eng, R. McNab, R. Inglis, T. J. Penfold, E. K. Brechin and J. O. Johansson, *Nat. Chem.*, 2020, DOI: 10.1038/s41557-020-0431-6.
72. C.-J. Yu, S. von Kugelgen, M. D. Krzyaniak, W. Ji, W. R. Dichtel, M. R. Wasielewski and D. E. Freedman, *Chem. Mat.*, 2020, **32**, 10200-10206.
73. F. Santanni, A. Albino, M. Atzori, D. Ranieri, E. Salvadori, M. Chiesa, A. Lunghi, A. Bencini, L. Sorace, F. Totti and R. Sessoli, *Inorg. Chem.*, 2021, **60**, 140-151.
74. L. Gu and R. Wu, *Phys. Rev. Lett.*, 2020, **125**, 117203.
75. M. Atzori, S. Benci, E. Morra, L. Tesi, M. Chiesa, R. Torre, L. Sorace and R. Sessoli, *Inorg. Chem.*, 2018, **57**, 731-740.
76. L. Tesi, E. Lucaccini, I. Cimatti, M. Perfetti, M. Mannini, M. Atzori, E. Morra, M. Chiesa, A. Caneschi, L. Sorace and R. Sessoli, *Chem. Sci.*, 2016, **7**, 2074-2083.
77. M. Atzori, L. Tesi, S. Benci, A. Lunghi, R. Righini, A. Taschin, R. Torre, L. Sorace and R. Sessoli, *J. Am. Chem. Soc.*, 2017, **139**, 4338-4341.
78. S. Sproules, *Dalton Trans.*, 2021, **50**, 4778-4782.
79. I. Gimeno, A. Urtizberea, J. Román-Roche, D. Zueco, A. Camón, P. J. Alonso, O. Roubeau and F. Luis, *Chem. Sci.*, 2021, **12**, 5621-5630.
80. A. Albino, S. Benci, L. Tesi, M. Atzori, R. Torre, S. Sanvito, R. Sessoli and A. Lunghi, *Inorg. Chem.*, 2019, **58**, 10260-10268.
81. E. Garlatti, L. Tesi, A. Lunghi, M. Atzori, D. J. Voneshen, P. Santini, S. Sanvito, T. Guidi, R. Sessoli and S. Carretta, *Nat. Commun.*, 2020, **11**, 1751.
82. R. Boča, C. Rajnák, J. Titiš and D. Valigura, *Inorg. Chem.*, 2017, **56**, 1478-1482.

83. H.-H. Cui, W. Lv, W. Tong, X.-T. Chen and Z.-L. Xue, *Eur. J. Inorg. Chem.*, 2019, **2019**, 4653-4659.
84. M. Dolai, M. Ali, C. Rajnák, J. Titiš and R. Boča, *New J. Chem.*, 2019, **43**, 12698-12701.
85. A. Mielcarek, A. Bieńko, P. Saramak, J. Jezierska and A. Dołęga, *Dalton Trans.*, 2019, **48**, 17780-17791.
86. M. Warner, S. Din, I. S. Tupitsyn, G. W. Morley, A. M. Stoneham, J. A. Gardener, Z. Wu, A. J. Fisher, S. Heutz, C. W. M. Kay and G. Aeppli, *Nature*, 2013, **503**, 504-508.
87. K. Bader, M. Winkler and J. van Slageren, *Chem. Comm.*, 2016, **52**, 3623-3626.
88. A. Urtizberea, E. Natividad, P. J. Alonso, M. A. Andrés, I. Gascón, M. Goldmann and O. Roubeau, *Adv. Funct. Mater.*, 2018, **28**, 1801695.
89. C.-J. Yu, M. D. Krzyaniak, M. S. Fataftah, M. R. Wasielewski and D. E. Freedman, *Chem. Sci.*, 2019, **10**, 1702-1708.
90. S. von Kugelgen, M. D. Krzyaniak, M. Gu, D. Puggioni, J. M. Rondinelli, M. R. Wasielewski and D. E. Freedman, *J. Am. Chem. Soc.*, 2021, **143**, 8069-8077.
91. Y. Dai, Y. Fu, Z. Shi, X. Qin, S. Mu, Y. Wu, J.-H. Su, Y.-F. Deng, L. Qin, Y.-Q. Zhai, Y.-Z. Zheng, X. Rong and J. Du, *Chin. Phys. Lett.*, 2021, **38**, 030303.
92. M. S. Fataftah, M. D. Krzyaniak, B. Vlaisavljevich, M. R. Wasielewski, J. M. Zadrozny and D. E. Freedman, *Chem. Sci.*, 2019, **10**, 6707-6714.
93. S. Lenz, K. Bader, H. Bamberger and J. van Slageren, *Chem. Commun.*, 2017, **53**, 4477-4480.
94. X. Liang, T.-Y. Zhang, X.-Y. Zeng, Y. Zheng, K. Wei and Y.-R. Yang, *J. Am. Chem. Soc.*, 2017, **139**, 3364-3367.
95. G. Huang, B. Kling, F. H. Darras, J. Heilmann and M. Decker, *Eur. J. Med. Chem.*, 2014, **81**, 15-21.
96. Y.-Y. Huang, C. Cai, X. Yang, Z.-C. Lv and U. Schneider, *ACS Catal.*, 2016, **6**, 5747-5763.
97. H. Li, K. M. Belyk, J. Yin, Q. Chen, A. Hyde, Y. Ji, S. Oliver, M. T. Tudge, L.-C. Campeau and K. R. Campos, *J. Am. Chem. Soc.*, 2015, **137**, 13728-13731.
98. G. Li, F. R. Fronczek and J. C. Antilla, *J. Am. Chem. Soc.*, 2008, **130**, 12216-12217.
99. J. Lu, F. Sha and X.-Y. Wu, *Tetrahedron Lett.*, 2019, **60**, 1161-1165.
100. T. Arai, K. Tsuchiya and E. Matsumura, *Org. Lett.*, 2015, **17**, 2416-2419.
101. S. Alvarez, P. Alemany, D. Casanova, J. Cirera, M. Llunell and D. Avnir, *Coord. Chem. Rev.*, 2005, **249**, 1693-1708.
102. D. C. M. Llunell, J.Cirera, P.Alemanyand and S.Alvarez, *Shape v.2.0*, Universitat de Barcelona, 2010.
103. M. Pinsky and D. Avnir, *Inorg. Chem.*, 1998, **37**, 5575-5582.
104. S. Khan, S. Herrero, R. González-Prieto, M. G. B. Drew, S. Banerjee and S. Chattopadhyay, *New J. Chem.*, 2018, **42**, 13512-13519.
105. W. Haase, *Ber. Bunsenges. Phys. Chem.*, 1994, **98**, 1208-1208.
106. N. F. Chilton, R. P. Anderson, L. D. Turner, A. Soncini and K. S. Murray, *J. Comput. Chem.*, 2013, **34**, 1164-1175.
107. K. S. Cole and R. H. Cole, *J. Chem. Phys.*, 1941, **9**, 341-351.
108. Y.-N. Guo, G.-F. Xu, Y. Guo and J. Tang, *Dalton Trans.*, 2011, **40**, 9953-9963.
109. M. Atzori, E. Morra, L. Tesi, A. Albino, M. Chiesa, L. Sorace and R. Sessoli, *J. Am. Chem. Soc.*, 2016, **138**, 11234-11244.
110. R. Boča, C. Rajnák, J. n. Moncol, J. n. Titiš and D. a. Valigura, *Inorg. Chem.*, 2018, **57**, 14314-14321.
111. C.-Y. Lin, T. Ngendahimana, G. R. Eaton, S. S. Eaton and J. M. Zadrozny, *Chem. Sci.*, 2019, **10**, 548-555.
112. F. Aquilante, J. Autschbach, R. K. Carlson, L. F. Chibotaru, M. G. Delcey, L. De Vico, I. Fdez. Galván, N. Ferré, L. M. Frutos, L. Gagliardi, M. Garavelli, A. Giussani, C. E. Hoyer, G. Li Manni, H. Lischka, D. Ma, P. Å. Malmqvist, T. Müller, A. Nenov, M. Olivucci, T. B. Pedersen, D. Peng, F. Plasser, B. Pritchard, M. Reiher, I. Rivalta, I. Schapiro, J. Segarra-Martí, M. Stenrup, D. G. Truhlar, L. Ungur, A. Valentini, S. Vancoillie, V. Veryazov, V. P. Vysotskiy, O. Weingart, F. Zapata and R. Lindh, *J. Comput. Chem.*, 2016, **37**, 506-541.
113. A. N. M., *Principles of electron spin resonance*, Prentice Hall, 1993.
114. H. Husein Mor, H. Weihe and J. Bendix, *J. Magn. Reson.*, 2010, **207**, 283-286.
115. B. J. Hathaway and D. E. Billing, *Coord. Chem. Rev.*, 1970, **5**, 143-207.
116. P. Sivaprasad, K. Ramesh and Y. P. Reddy, *Phys. Status Solidi B*, 1990, **118**, K103-K106.
117. D. E. Billing, R. J. Dudley, B. J. Hathaway and A. A. G. Tomlinson, *J. Chem. Soc. A*, 1971, DOI: 10.1039/J19710000691, 691-696.
118. E. Garribba and G. Micera, *J. Chem. Educ.*, 2006, **83**, 1229.
119. P. P. M. Valko, S. Biskupič, and M. Mazúr, *Chem. Pap.*, 1990, **44**, 805-813.
120. D. Ganyushin and F. Neese, *J. Chem. Phys.*, 2006, **125**, 024103.
121. F. Neese, *WIRES Comput. Mol. Sci.*, 2012, **2**, 73-78.
122. S. Grimme, *J. Chem. Phys.*, 2013, **138**, 244104.
123. C. Bannwarth and S. Grimme, *Comput. Theo. Chem.*, 2014, **1040-1041**, 45-53.
124. S. Hirata and M. Head-Gordon, *Chem. Phys. Lett.*, 1999, **314**, 291-299.
125. A. Abragam and B. Bleaney, *Electron Paramagnetic Resonance of Transition Ion*, Clarendon Press, Oxford, 1970.
126. S. K. Misra, *Ed. Multifrequency Electron Paramagnetic Resonance; Erratum S.K. Misra, C. Rudowicz, http://www.wiley-vch.de/publish/dt/books/ISBN3-527-40779-0/*. Wiley-VCH, Weinheim 2011.
127. A. Drzewiecki, B. Padlyak, V. Adamiv, Y. Burak and I. Teslyuk, *Nukleonika*, 2013, **58**, 379--385.
128. J. L. Rao, G. Sivaramaiah and N. Gopal, *Physica B*, 2004, **349**, 206-213.
129. R. Ravikumar, R. Komatsu, K. Ikeda, A. Chandrasekhar, B. Reddy, Y. Reddy and P. S. Rao, *J. Phys. Chem. Solids*, 2003, **64**, 261-264.
130. M. Atanasov, D. Ganyushin, K. Sivalingam and F. Neese, in *Molecular Electronic Structures of Transition Metal Complexes II*, eds. D. M. P. Mingos, P. Day and J. P. Dahl, Springer Berlin Heidelberg, Berlin, Heidelberg, 2012, DOI: 10.1007/430_2011_57, pp. 149-220.
131. E. A. Suturina, D. Maganas, E. Bill, M. Atanasov and F. Neese, *Inorg. Chem.*, 2015, **54**, 9948-9961.
132. Z. Wen-Chen and W. Shao-Yi, *Z. Naturforsch.*, 2000, **55**, 915-917.
133. M.-Q. Kuang, L.-D. Wang and S.-K. Duan, *J. Phys. Chem. Solids*, 2017, **111**, 41-46.
134. H.-M. Zhang and X. Wan, *J. Non-Cryst. Solids*, 2013, **361**, 43-46.
135. S.-Y. Wu, H.-M. Zhang, P. Xu and S.-X. Zhang, *Spectrochim. Acta A*, 2010, **75**, 230-234.

136. M.-Q. Kuang, S.-Y. Wu, G.-L. Li and X.-F. Hu, *Mol. Phys.*, 2015, **113**, 698-702.
137. S. Y. WU, J. S. YAO, H. M. Zhang and G. D. LU, *Int. J. Mod. Phys. B*, 2007, **21**, 3250-3253.
138. K. Min-Quan, W. Shao-Yi, H. Xian-Fen and S. Bo-Tao, *Z. Naturforsch. A*, 2013, **68**, 442-446.
139. L. Chao-Ying, H. Ying and Z. Xue-Mei, *Physica B*, 2015, **456**, 125-128.
140. M.-Q. Kuang, S.-Y. Wu and H.-M. Zhang, *Optik*, 2012, **123**, 1601-1604.
141. M.-Q. Kuang, S.-Y. Wu, X.-F. Hu and B.-T. Song, *Physica B*, 2013, **417**, 13-16.
142. D. J. Newman and B. Ng, *Rep. Prog. Phys.*, 1989, **52**, 699-762.
143. C. A. Morrison, in *Crystal Fields for Transition-Metal Ions in Laser Host Materials*, ed. C. A. Morrison, Springer Berlin Heidelberg, Berlin, Heidelberg, 1992, DOI: 10.1007/978-3-642-95686-7_1, pp. 1-2.
144. B. G. Wybourne, *Spectroscopic Properties of Rare Earths*, Interscience Publishers, 1965.
145. C. Rudowicz, *Crystal Field Handbook*, 2000, **259**.
146. C. Rudowicz and Q. Jian, *Comput. & Chem.*, 2002, **26**, 149-157.
147. C. Rudowicz and R. Bramley, *J. Chem. Phys.*, 1985, **83**, 5192-5197.
148. C. Rudowicz and P. Gnutek, *Physica B*, 2010, **405**, 113-132.
149. J. S. Griffith, *The theory of transition-metal ions*, Cambridge University Press, 1964.
150. Y. Y. Yeung and C. Rudowicz, *Comput. & Chem.*, 1992, **16**, 207-216.
151. G. W. Burdick and M. F. Reid, *Mol. Phys.*, 2004, **102**, 1141-1147.
152. M. Karbowiak, C. Rudowicz and P. Gnutek, *Opt. Mater.*, 2011, **33**, 1147-1161.
153. M. Karbowiak, P. Gnutek and C. Rudowicz, *Chem. Phys.*, 2012, **400**, 29-38.
154. M. Kozanecki, C. Rudowicz, H. Ohta and T. Sakurai, *J. Alloys Compd.* , 2017, **726**, 1226-1235.
155. M. Kozanecki and C. Rudowicz, *J. Magn. Magn. Mater.* , 2020, **493**, 165670.
156. S. Gómez-Coca, A. Urtizberea, E. Cremades, P. J. Alonso, A. Camón, E. Ruiz and F. Luis, *Nat. Commun.*, 2014, **5**, 1-8.

Insert Table of Contents artwork here

Modular organic scaffold for magneto-structural correlation studies

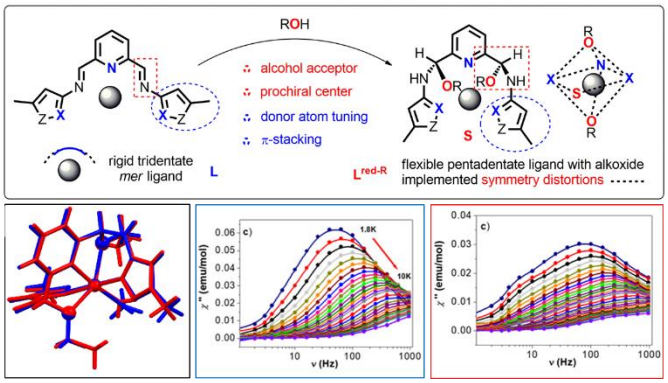

Novel organic scaffold that would allow to gain insight into how subtle structural differences affect the slow magnetic relaxation in *S* = ½ systems.